

Quantum computer-aided design: digital quantum simulation of quantum processors

Thi Ha Kyaw,^{1,2,*} Tim Menke,^{3,4,5,*} Sukin Sim,⁶ Nicolas P. D. Sawaya,⁷
William D. Oliver,^{4,8} Gian Giacomo Guerreschi,⁷ and Alán Aspuru-Guzik^{1,2,9,10,†}

¹*Department of Computer Science, University of Toronto, Toronto, Ontario M5S 2E4, Canada*

²*Department of Chemistry, University of Toronto, Toronto, Ontario M5G 1Z8, Canada*

³*Department of Physics, Harvard University, Cambridge, MA 02138, USA*

⁴*Research Laboratory of Electronics, Massachusetts Institute of Technology, Cambridge, MA 02139, USA*

⁵*Department of Physics, Massachusetts Institute of Technology, Cambridge, MA 02139, USA*

⁶*Department of Chemistry and Chemical Biology,
Harvard University, Cambridge, MA 02138, USA*

⁷*Intel Labs, Santa Clara, California 95054, USA*

⁸*Department of Electrical Engineering and Computer Science,
Massachusetts Institute of Technology, Cambridge, MA 02139, USA*

⁹*Vector Institute for Artificial Intelligence, Toronto, Ontario M5S 1M1, Canada*

¹⁰*Canadian Institute for Advanced Research, Toronto, Ontario M5G 1Z8, Canada*

(Dated: April 4, 2022)

With the increasing size of quantum processors, the sub-modules that constitute the processor will become too large to accurately simulate on a classical computer. Therefore, one would soon have to fabricate and test each new design primitive and parameter choice in time-consuming coordination between design, fabrication, and experimental validation. To circumvent this slow-down, we address the question of how one can design and test the performance of next-generation quantum hardware – by using existing quantum computers. Focusing on superconducting transmon processors as a prominent hardware platform, we compute the static and dynamic properties of individual and coupled transmons. We show how the energy spectra of transmons can be obtained by variational hybrid quantum-classical algorithms that are well-suited for near-term noisy quantum computers. We also numerically demonstrate how single- and two-qubit gates can be simulated via Suzuki-Trotter decomposition for digital quantum simulation. Our methods pave a new way towards designing candidate quantum processors when the demands of calculating sub-module properties exceed the capabilities of classical computing resources.

* These authors contributed equally to this work. thihakyaw@cs.toronto.edu tim_menke@g.harvard.edu

† alan@aspuru.com

I. INTRODUCTION

In the semiconductor industry, next-generation microprocessors are developed using existing computers and a variety of software tools for hardware description and simulation [1–5]. During this design process, it has been established that a *less* powerful processor or a collection of such processors is capable of aiding the design of a novel and *more* powerful processor. The existing processor does not need to fully simulate the next-generation one; it suffices to use the current processor to understand and validate design primitives of the future processor’s sub-modules. We refer to a sub-module as tightly linked circuitry that shares a relatively large amount of wiring, forms a small building block on its own, and is often repeated throughout the processor. Drawing a parallel with the rising industry of manufacturing quantum computing devices, we observe that, thus far, their sub-module design and simulation have been performed on classical computers [6–10]. The resource requirements for such classical simulations scale exponentially with the number of simulated hardware qubits as well as with the number of energy levels included per qubit. For example, transmon qubits for superconducting circuit quantum computation have low anharmonicity between the energy levels, and inclusion of additional states beyond the computational states is important to understand the device characteristics and implement high-fidelity control pulses [8]. As a result, classical simulations of quantum computing hardware are limited to a small number of qubits, even when employing the most powerful supercomputers. With the rise of quantum processors, hardware simulations are already becoming infeasible. We contend that this simulation challenge can be addressed by simulating the quantum processor hardware on a quantum computer. In this way, we restore the symmetry between design platform and designed platform that is known from the semiconductor industry: Future-generation quantum computers need to be designed with the aid of existing quantum computers.

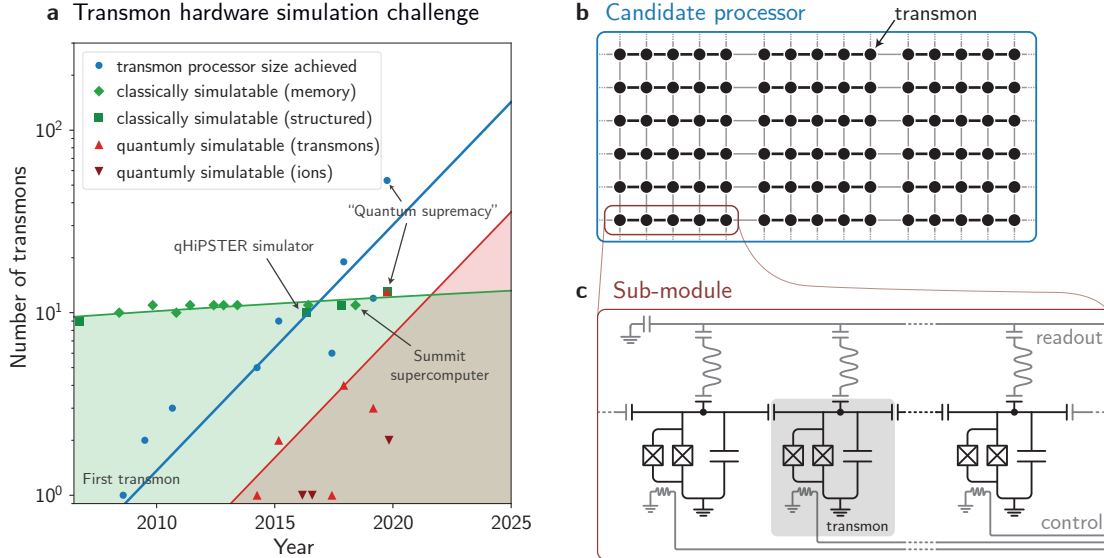


FIG. 1. The challenge of simulating transmon quantum processors. (a) The historical numbers of transmons in a superconducting processor suggests an exponential growth in processor size, while classical supercomputer simulations will be limited to about ten transmons in the foreseeable future. Quantum computers will soon be able to simulate larger transmon processors than their classical counterparts. The blue dots show the size of a selection of published transmon processors over time (Refs. [11–19] chronologically). The green diamonds show the maximum number of transmons that the best supercomputer at the given point in time could simulate based naïvely on its memory size [20]. Another estimate for the classically simulatable processor size takes the maximum number of data qubits for which a quantum algorithm has been simulated on a supercomputer and scales it to the number of transmons that these qubits could encode (green squares, Refs. [21–23],[19] chronologically). The red triangles show the number of transmons that could be simulated on an experimentally demonstrated quantum computer that is made up of transmons themselves (triangles up, Refs. [14–19] chronologically) or of ions (triangles down, Refs. [24–26] chronologically). All solid lines are to guide the eye along the general trend of the transmon processor size (blue), classically simulatable processor size (green), and quantumly simulatable processor size (red). Note that the cost of simulation is a constant offset in this log-linear plot and grows as fast as the available quantum processors. (b) Design proposals for new processors typically consist of tiled sub-modules (red box) that share common readout circuitry and that can be perceived as the unit cells of the processor. (c) This work considers the case in which the sub-modules are chains of capacitively coupled transmons, for which the circuit diagram including readout and flux control circuitry is shown here.

We present methodology for quantum computer-aided design for the example of superconducting transmon qubits,

which are one of the leading hardware platforms for digital quantum computation [8]. In this way, we are able to develop explicit quantum algorithms for hardware simulation, provide resource counts, and give a quantitative estimate for when quantum hardware simulation capabilities will surpass those of classical simulations. As shown in Fig. 1(a), the number of transmons in experimentally demonstrated processors grows at an exponential pace. A selection of processors that are capable of shallow algorithms or processor-wide entanglement is visualized, from the first demonstration of a transmon qubit in 2008 [11] up to the “quantum supremacy” experiment in 2019 [19]. The evident exponential trend in transmon processor size has also been discussed in popular scientific discourse [27].

We contrast the growth of the transmon processor size with the number of transmons that can be simulated on a classical computer. A numerically accurate simulation of a transmon qubit circuit requires inclusion of about $2^4 = 16$ basis states of the quantum circuit. Other basis states can be neglected because they do not significantly contribute to the relevant low energy eigenstates. Therefore, the truncated Hilbert space of a processor with M transmons has dimension 16^M . In Fig. 1(a), it is shown that the memory size of the most powerful supercomputers is sufficient to store the relevant state space of only about ten coupled transmons. As each additional transmon requires a 16-fold increase in memory, the effective increase in transmon simulation capacity of supercomputers has been slow over the past decade. In fact, while the supercomputer “Roadrunner” in 2008 was able to store the relevant state space of ten coupled transmons, today’s best machine “Summit” can store the state space of only one additional transmon in its memory. However, the structure of a quantum computation problem can often be exploited to reduce the classical simulation resource requirements. Since we are unaware of prior work on simulating large transmon processors at the hardware level that captures the multi-level nature of the circuit, we turn to the related application of simulating quantum algorithms on abstract qubits. Classical supercomputers have been able to simulate algorithms with up to 53 qubits if the algorithm connects most but not all of Hilbert space [19, 21–23]. It is conceivable that similar techniques can be used to simulate the quantum algorithms for transmon hardware that we present in this work. Given the cost of encoding the multi-level nature of a hardware transmon, the classical simulation capacity would be reduced by a factor of four when simulating hardware transmons rather than abstract qubits. The resulting *structured* classical simulation capacity is shown in Fig. 1(a) and is still on the order of ten transmons. More drastic reductions in classical resource requirements are possible if one reduces the Hilbert space size and tolerates simulation errors or restricts the state space. In the context of superconducting circuits, Di Paolo *et al.* have computed the lowest-lying states of a many-mode fluxonium qubit using a tensor network approach [28]. Such techniques hold great promise for extracting the interaction of a few low lying excitations in the many-body system, for example to determine the amount of crosstalk between pairs of transmons. Tensor network approaches, however, do not usually converge well for system dimensions greater than one [29]. Hence, it is unclear whether classical simulations of superconducting circuit elements based on the density matrix renormalization group technique (DMRG) [30, 31] would prevail if the underlying superconducting circuit design extends to two or more dimensions. For general quantum states, DMRG algorithms require a bond dimension scaling that is exponential in the number of active nodes in the circuit. The method presented here would not have such aforementioned limitations. In addition, if one seeks to study a fully interacting transmon processor with single-qubit control and all-to-all entanglement generation, the lowest-energy states of each transmon need to be included in the simulation. The classical resource requirement therefore continues to grow exponentially with the number of transmons, albeit at a different rate. As a result, the classically simulatable transmon processor size on the semi-logarithmic scale of Fig. 1(a) is shifted up by a constant number but the slope is unchanged. Transmon processor growth still outpaces classical simulation capabilities exponentially in this scenario. Overall, these trends illustrate the challenge of how quantum properties of new quantum processor designs can be validated computationally before they are passed on to the cost- and time-intensive fabrication and experimental testing stages.

Digital quantum simulation has been shown to hold promise for the understanding of quantum systems ranging from quantum chemistry applications [16, 32, 33] over many-body systems [34–36] to quantum field theories [37, 38], among others [39]. In fact, it has been advocated for as one of the main applications of quantum computing [34, 40]. In this work, we provide a path towards overcoming classical limitations of quantum processor simulation by developing the new paradigm of simulating quantum computing hardware using quantum computers. As an example of this approach, we develop methods to simulate the building blocks of a superconducting transmon processor on a digital quantum computer. On a quantum computer, the 16 transmon energy levels that are required for numerically accurate simulation can be represented by four data qubits. The quantum resource requirement for simulating transmon processors is therefore linear in the number of transmons, and one more transmon can be simulated for each additional four data qubits on the simulating processor. In Fig. 1(a), it is shown how many transmons recent superconducting and ion based digital quantum computers could simulate, based on their number of qubits, i.e. we divide the number of qubits in these processors by four. Again, we emphasize that these processors are all capable of executing shallow digital quantum algorithms or generating processor-wide entanglement. Thus, at least a shallow variational algorithm to determine transmon properties as described in this work could conceivably be run on them. The quantumly simulatable transmon processor size naturally follows the demonstrated experimental transmon

processor size, as new digital processors can again be employed to simulate smaller processor hardware. Therefore, the quantum simulation capacity for transmon processors grows much more rapidly than the classical simulation capacity. Based on the general trends that we identify in Fig. 1(a), digital quantum computers will be able to simulate more transmons than classical computers within the next few years.

An exemplary design primitive for a transmon processor sub-module is shown in Fig. 1(b-c): A chain of capacitively coupled transmons with a common readout line is tiled to construct a large quantum processor. Here we employ near-term hybrid variational quantum-classical algorithms to find the energy spectrum of one- and two-transmon cells of such a quantum sub-module (see Sec. III A and Sec. III B). The spectrum allows for validation of the design and determination of the system's operating points, and the optimized variational algorithms supply state preparation routines for the computational basis states. Consequently, high-fidelity one- and two-transmon operations are tuned up and benchmarked using Suzuki-Trotter evolution: A single-qubit bit-flip gate is implemented via the derivative removal by adiabatic gates (DRAG) scheme [41] (see Sec. III A), and the two-qubit controlled phase (CPHASE) gate is realized with a non-adiabatic flux sweep to an avoided level crossing [12, 42] (see Sec. III B). Convergence rates and gate counts of the employed algorithms are used to extrapolate resource requirements for the quantum simulation of complete sub-modules (see Sec. III C). The concepts applied in this work are generalizable to other transmon-based quantum hardware as well as to simulating the realistic multi-state nature of trapped ion [43], neutral atom [44], and photonic systems [45]. In a separate and similar line of work, some of us target quantum computer aided design of quantum optical hardware, translating corresponding unitary operators to digital quantum circuits [46].

II. METHODS FOR QUANTUM SIMULATION OF TRANSMON PROCESSORS

We consider the fundamental unit of a superconducting quantum processor as a physical quantum system that is approximately operated in its two lowest-lying eigenstates (a qubit). Throughout this work, we use the term *physical qubit* to refer to the hardware qubit that is being simulated, the one we aim to design for the next-generation processor. The physical qubit variant considered here is the superconducting transmon qubit [47], and the terms *physical qubit* and *transmon* are used interchangeably. To perform the hardware simulation, we employ *data qubits* in near- and medium-term quantum computers to digitally simulate one or more physical qubits. The data qubits are architecture-independent.

We propose a three-step process to simulate a transmon processor with digital data qubits. First, the transmon Hamiltonian is translated into the language of digital quantum computers, that is in terms of Pauli strings (see Sec. II A). The mapping to Pauli strings employed in this study is the resource efficient Gray encoding [48], which is summarized in Appendix C and discussed in detail in Ref. [49]. Second, the eigenstates of the circuit are determined using variational hybrid quantum-classical algorithms including the variational quantum eigensolver (VQE) [50, 51] and the variational quantum deflation algorithm (VQD) [52], which are described in Sec. II B. Lastly, Suzuki-Trotter evolution [53] as reviewed in Sec. II C is performed to simulate the time evolution of high fidelity single- and two-qubit gate operations. We note that the eigenstates that were variationally determined can be used as initial states for the time evolution. In order to operate a quantum processor, one also needs to consider readout and undesired coupling to the environment. Readout capability, for instance, is indicated by the resonator that is connected to all sub-module transmons in Fig. 1(b). The simulation of readout and environment effects is beyond the scope of this work but they may be simulated by adding couplings to the appropriate environment variables in the simulated Hamiltonian.

A. Encoding of circuit Hamiltonians into multi-qubit operators

We choose a sub-module that corresponds to a chain of M capacitively coupled transmons as shown in Fig. 1(c). Each transmon is associated with a circuit node that is indicated by a circular dot in the circuit diagram. The sub-module choice is motivated by a conceivable processor in which all transmons in a chain are coupled to a common readout resonator, and the separate chains that constitute the processor have weak intra-chain coupling. Within a chain, the presence of the resonator adds to the capacitive cross-talk between the qubits and can lead to unwanted or uncontrolled coupling effects [54]. The inter-chain couplings would be weaker and better controlled by comparison, so a focus on the isolated chain as a sub-module instance is warranted.

The transmon chain is described by the following Hamiltonian:

$$\hat{H}_{M\text{-transmon}} = 2e^2 \sum_{i,j=1}^M (\mathbf{C}^{-1})_{ij} \hat{N}_i \hat{N}_j - 2 \sum_{i=1}^M E_{J,i} |\cos(2\pi f_i)| \cos \hat{\phi}_i. \quad (1)$$

Here, e is the electron charge. The normalized external flux $f_i = \Phi_{\text{ext},i}/\Phi_0$ is derived from the external magnetic flux $\Phi_{\text{ext},i}$ that penetrates the loop formed by the two Josephson junctions of each transmon. The Josephson energy of the two junctions is equal and given by $E_{J,i}$. The magnetic flux quantum Φ_0 is a fundamental constant that describes the smallest amount of flux that a superconducting loop can sustain. The Hamiltonian is written in terms of the canonically conjugate phase operators $\hat{\varphi}_i$ and number operators \hat{N}_i for the transmon with index $i \in \{1, \dots, M\}$. They fulfill the commutation relation $[\hat{\varphi}_i, \hat{N}_j] = i\delta_{ij}$. These operators are related to the flux operator $\hat{\Phi}_i = \Phi_0 \hat{\varphi}_i / 2\pi$, which denotes the flux across the Josephson junction of qubit i , and the charge operator $\hat{Q}_i = 2e\hat{N}_i$ that describes the sum of charges stored on all capacitors connected to the qubit [7]. The capacitance matrix \mathbf{C} is determined from the Legendre transformation of the circuit Lagrangian. It contains the sum of all capacitances connected to a node on the diagonal and minus one times the capacitance between two nodes on the off-diagonal. The interaction of transmons in the chain is determined by the inverse capacitance matrix \mathbf{C}^{-1} , which couples their charge degrees of freedom. Although \mathbf{C} is tridiagonal for a chain, its inverse is not. Instead, for realistic parameter settings, it is a full matrix with exponentially decaying elements away from the diagonal. Therefore, nearest-neighbor capacitances lead to non-nearest-neighbor interactions. In addition, spurious capacitances such as those arising from a readout resonator as discussed above can lead to enhanced coupling between non-nearest-neighbor sites [54]. To investigate such effects prior to chip fabrication, simulation of multiple coupled transmons is necessary. This is one of the motivations for this work on quantum simulation techniques for sub-module sizes that cannot be precisely simulated classically.

To numerically demonstrate quantum simulation of transmon sub-modules, we restrict ourselves to one-transmon (see Fig. 2(a)) and two-transmon (see Fig. 4(a)) circuits. This is sufficient to showcase quantum computation of static transmon properties as well as dynamic simulation of single-qubit and entangling gates. In Sec. III C we discuss how the simulation techniques scale to multi-transmon chains. Here we state the 1-transmon and 2-transmon Hamiltonians, which are the $M = 1$ and $M = 2$ special cases of Eq. (1):

$$\hat{H}_{1\text{-transmon}} = 4E_C \hat{N}^2 - 2E_J |\cos(2\pi f)| \cos \hat{\varphi}, \quad (2)$$

$$\hat{H}_{2\text{-transmon}} = 4E_C(1 + \xi)^{-1}(\hat{N}_1^2 + \hat{N}_2^2 + 2\xi \hat{N}_1 \hat{N}_2) - 2E_{J,1} |\cos(2\pi f_1)| \cos \hat{\varphi}_1 - 2E_{J,2} |\cos(2\pi f_2)| \cos \hat{\varphi}_2. \quad (3)$$

The parameter $E_C = e^2/2(C_{\text{sh}} + C_J)$ is the charging energy and $\xi = C_c/(C_c + C_{\text{sh}} + C_J)$. We note that the labelling 1, 2 in the Hamiltonian $\hat{H}_{2\text{-transmon}}$ is not limited to nearest-neighbour transmons, but the two transmons can in principle be separated by some other transmons within the same single sub-module [55].

The single and coupled transmon Hamiltonians can be described as a single and pair of non-linear oscillators, respectively, with an infinite number of level excitations; the degrees of freedom of superconducting circuits are bosonic in nature. However, only the low-lying energy states are relevant when the transmon qubit is operated at millikelvin temperatures, given the typical excitation frequencies. By truncating the Hilbert space to a finite dimension, we can map Eqs. (2) and (3) to respective Hamiltonians expressed as the linear combination of products of Pauli operators. These Hamiltonians are defined based on data qubits of a digital quantum computer that we propose to use for designing the novel transmon-based quantum sub-module. Based on the Hamiltonian truncation employed in exact diagonalization, we find that four data qubits are needed to simulate a single transmon physical qubit with sufficient accuracy if one is interested only in low energy excitation modes. In Appendix B, we discuss how to represent the operators of $\hat{H}_{1\text{-transmon}}$ and $\hat{H}_{2\text{-transmon}}$ in the charge basis first, and then transform them into a linear combination of Pauli strings in Appendix C. The Hamiltonian then assumes the form $\hat{H} = \sum_i \hat{h}_i$, where each term \hat{h}_i is a tensor product of multiple Pauli and identity operators, scaled by a prefactor. While several possible mappings are available for the Pauli string transformation [56], the Gray encoding is resource-efficient for the types of operators we consider as is used throughout this work.

B. Variational quantum algorithm for multi-level systems

With the transmon Hamiltonian rephrased in terms of qubit operators, one can estimate its eigenenergies with high accuracy by employing the variational quantum eigensolver (VQE) algorithm [50, 51], a hybrid quantum-classical algorithm designed to compute properties of Hermitian operators using current and near-term quantum devices. Early implementations of VQE have focused on estimating the ground state energy of quantum systems: The quantum device is used to prepare the candidate state by executing a parameterized quantum circuit \hat{U}_θ whose parameter values θ are updated using classical optimizers. The classical optimization is guided by minimizing the energy expectation of the candidate state, usually estimated by averaging measurements from many runs of the same circuit. The objective of VQE can be expressed as

$$\min_{\theta} \langle \psi_\theta | \hat{H} | \psi_\theta \rangle, \quad (4)$$

where \hat{H} corresponds to the system Hamiltonian [57], θ corresponds to the vector of circuit parameters, and $|\psi_\theta\rangle = \hat{U}_\theta|\phi_0\rangle$ is the resulting quantum state parameterized by θ , where $|\phi_0\rangle$ is a reference state. Instances of the VQE algorithm have been demonstrated using various quantum computing architectures including superconducting circuits [16, 58], trapped ions [59–61], and photonic chips [50]. In recent years, the VQE algorithm has been generalized to estimate low-lying excited states in addition to the ground state [52, 62]. In the latter work, the original objective function in VQE is extended such that the k -th excited state can be systematically estimated. This is crucial in determining higher energy levels of superconducting transmon systems which are needed to generate high fidelity one- and two-qubit gate operations (see Sec. III). Similar to the VQE cost function, the objective for the k -th excited state of the so-called “Variational Quantum Deflation” (VQD) algorithm [52] can be written as

$$\min_{\theta_k} \left(\langle \psi_{\theta_k} | \hat{H} | \psi_{\theta_k} \rangle + \sum_{i=0}^{k-1} \beta_i |\langle \psi_{\theta_k} | \psi_{\theta_i} \rangle|^2 \right), \quad (5)$$

where θ_k corresponds to the parameter setting that approximates the k -th excited state energy, and β_i are constants that penalize nonzero overlaps with previous eigenstate estimates. Given a large enough β_i , i.e. $\beta_i > E_k - E_i$ and a sufficiently flexible and efficient ansatz, the VQD objective can converge to E_k . A self-correcting procedure is suggested for choosing an appropriate value for β_i . This involves choosing a test parameter $\gamma := \beta_i + E_i$, such that if γ is too small, i.e. $\gamma - E_i = \beta_i \leq E_k - E_i$, the VQD algorithm outputs a minimum at γ . In such circumstances, we follow the recommended heuristic rule to double the value of γ . All VQE and VQD wavefunction simulations are implemented using OpenFermion [63] and Forest [64].

C. Suzuki-Trotter simulation of quantum gates

In addition to the static energy spectrum, simulating dynamical gate operations is an important aspect in the design of quantum hardware. The relevant metric for a hardware gate is the gate fidelity, which is a quantitative measure of how well a control pulse transforms an initial state $|\psi_0\rangle$ into a desired state $|\psi_{\text{des}}\rangle = \hat{U}_{\text{des}}|\psi_0\rangle$, where \hat{U}_{des} is the desired gate unitary. Since hardware gates exhibit a number of imperfections such as inducing leakage to higher excited states, state evolution under the control pulse will not precisely implement the desired unitary \hat{U}_{des} . The exact time evolution of the initial state $|\psi_0\rangle$ under the control pulse is written as $|\psi_{\text{ex}}(t)\rangle$. The gate fidelity is then defined as $F = |\langle \psi_{\text{ex}}(t_g) | \psi_{\text{des}} \rangle|^2$, where the gate time t_g is optimized to maximize the gate fidelity for a given control pulse. An estimate of the average gate fidelity \bar{F} over all states in the qubit Hilbert space is obtained by averaging the gate fidelity over sufficiently many Haar random initial state samples. For the hardware gates studied in this work, we simulate the numerically exact state evolution in QuTiP [65] in order to estimate the gate fidelities and provide an exact solution benchmark.

We investigate the use of Suzuki-Trotter evolution to simulate hardware gates on a digital quantum computer. With the first order Suzuki-Trotter approximation, the exact time evolution \hat{U}_{ex} under the control pulse becomes [66]

$$\hat{U}_{\text{ex}}(t) = \exp(-i\hat{H}t/\hbar) \approx \left[\prod_{i=1}^N \exp(-i\hat{h}_i t/\hbar K) \right]^K + \mathcal{O}(t^2/K) = \hat{U}_{\text{trot}}(t), \quad (6)$$

where K is the number of Trotter steps, \hbar is the reduced Planck constant, and each exponential of a weighted Pauli string \hat{h}_i is translated into a gate sequence on the digital quantum computer. The state evolution $|\psi_{\text{trot}}(t)\rangle = \hat{U}_{\text{trot}}(t)|\psi_0\rangle$ is simulated numerically using the Intel Quantum Simulator [22, 67]. In order to assess the resource requirements for Suzuki-Trotter simulations on digital quantum computers, it needs to be determined how the simulation error depends on the number of Trotter steps. While the theoretical error $\mathcal{O}(t^2/K)$ of the approximate time evolution operator provides an upper bound, numerical simulations can often tighten this bound [68]. We define the Trotter error of a specific simulation as $\mathcal{E} = 1 - |\langle \psi_{\text{trot}}(t_g) | \psi_{\text{ex}}(t_g) \rangle|^2$ and again approximate its average $\bar{\mathcal{E}}$ over the qubit Hilbert space by Haar random sampling of initial states. In Sec. III, we determine the scaling of $\bar{\mathcal{E}}$ with the number of Trotter steps and compare it against the theoretical bound.

The formulation of Eq. (6) assumes a time-independent Hamiltonian. In the case of a time-dependent Hamiltonian $\hat{H}(t)$ such as for the single-qubit pulse in Sec. III A, a time dependence needs to be added to the Pauli strings \hat{h}_i . The approximation error then also depends on the time derivative of the Hamiltonian [69]. As the time dependence in the single-qubit case is slow, we do not expect a large added error and refer to Refs. [66, 69, 70] for further information on time-dependent Suzuki-Trotter algorithms and error budgets.

III. RESULTS

This section is divided into two main subsections: single-qubit design and two-qubit gate design, each of which can then be subcategorized in terms of two functionalities each, namely initial state preparation via the VQE and VQD algorithms and Trotterized evolution to carry out dynamical quantum simulation. By “quantum computer-aided design” we refer to the use of quantum computers to generate the energy spectrum of the quantum device with high precision as well as to simulate its unitary dynamics in order to facilitate the design of quantum processors. Based on the energy spectrum, we can analyze whether or not the quantum device being designed is robust against some external controllable or uncontrolled parameters [71]. In addition, spectral information aids the design of desired quantum gates.

A. Single-qubit design

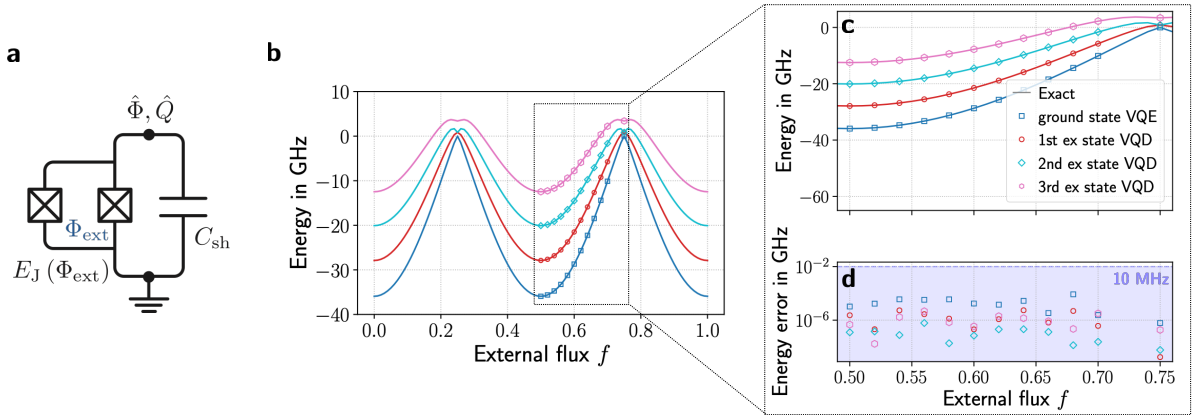


FIG. 2. (a) Circuit diagram of a transmon qubit with tunable external magnetic flux Φ_{ext} . (b) The four lowest eigenenergies are computed against the normalized external magnetic flux $f = \Phi_{\text{ext}}/\Phi_0$. The solid lines correspond to the exact diagonalization result, where the operators \hat{N} and $\hat{\varphi}$ are truncated to $d = 16$ states. In the quantum simulation, we use four data qubits to simulate one physical transmon. Using the VQE and VQD algorithms, the four lowest eigenenergies are estimated (colored markers) and plotted over exact values. (c) The quantumly simulated spectral region is magnified to emphasize the good agreement between quantum and classical simulation. (d) Energy errors of the respective VQE and VQD algorithms are plotted against f . Each dot represents the error incurred after completion of the algorithms and marker colors correspond to the legend of (c). The shaded region indicates an error threshold of 10 MHz and below.

As a first demonstration, we consider a flux tunable transmon consisting of a two-junction SQUID loop with junction energies $E_J/h = 20$ GHz, where h is the Planck constant, and capacitance $C_{\text{sh}} + C_J = 91$ fF (see Fig. 2(a)). The Josephson energy can be tuned by an external flux Φ_{ext} that is threading the SQUID loop and the entire system is described by the Hamiltonian in Eq. (2). From numerical diagonalization we determine that four data qubits accurately represent the low-lying states of one multilevel transmon, encoding the lowest 16 Cooper pair number states of the transmon. As we increase the number of data qubits and thus relax the Hilbert space truncation, the accuracy is increased. The four lowest eigenenergies obtained from numerically exact diagonalization are shown in Fig. 2(b).

We then employ the variational VQE and the VQD algorithms in order to estimate the same four lowest eigenenergies. Our method relies on abstract digital quantum gates and is applicable across quantum computing platforms, such as trapped ion or superconducting quantum processors. To highlight the applicability to trapped ions, we deploy a variational ansatz comprising single-qubit rotation gates followed by two-qubit Mølmer-Sørensen gates, which are native operations for trapped ion devices. Two layers of the four-qubit instance of the ansatz shown in Fig. D.3 are used to simulate the single transmon. The circuit template is inspired by Ref. [72] and is chosen based on high “expressibility” of the ansatz. For applying VQE and VQD to modest-sized systems in which the general structure of eigenstates is not well-understood, it may be helpful to use a highly expressible ansatz, where expressibility is defined as in Ref. [73]. For parameter updates, we employ the L-BFGS-B optimization routine [74]. A layer-wise training strategy for optimizing the circuit parameters is used, sequentially optimizing sets of parameters corresponding to layers in a multi-layered parameterized quantum circuit. The energy errors shown in Fig. 2(d) are computed as the

absolute difference between the variational values and those determined numerically via exact diagonalization. We remark that the energies are estimated to high accuracy, i.e. with errors falling below the threshold of 10 MHz, marked using a blue horizontal dotted line. For comparison, the energy difference between the ground and first excited states of a typical transmon is about 6 GHz [8]. Thus, the VQE and VQD errors are small with respect to the characteristic energy scale of the transmon.

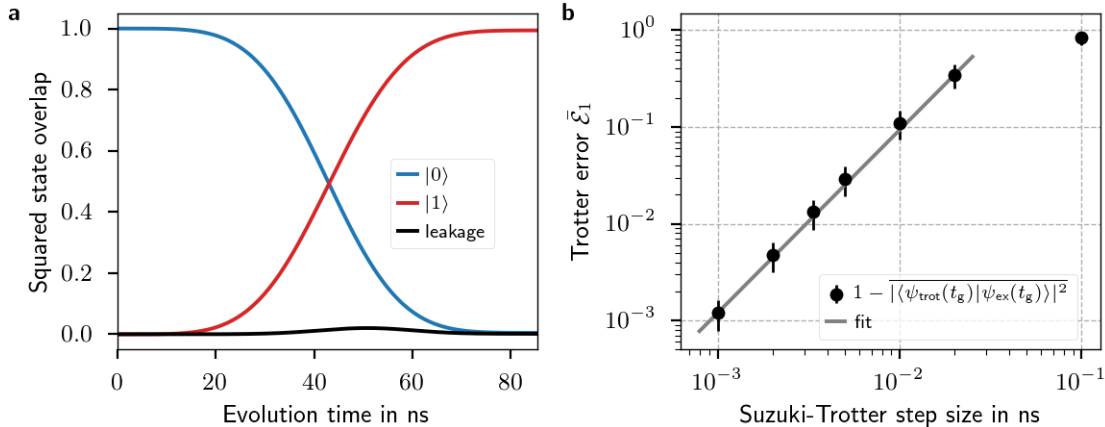


FIG. 3. Digital quantum simulation of a transmon bit-flip gate operation. (a) Population in the transmon computational basis states denoted as $|0\rangle$ and $|1\rangle$, as well as all other population in undesired states, labelled as “leakage”, are plotted against Trotterized evolution time. The transmon is driven by a DRAG pulse to undergo the bit-flip process. Only one dynamical instance involving 1000 Trotter steps is shown here. (b) Trotter error $\bar{\mathcal{E}}_1$ versus single step Trotter time. For each Trotter step size, we perform Suzuki-Trotter evolution under the DRAG pulse for time $t_{g1} = 85.32$ ns for 300 Haar random initial states spanned by $\{|0\rangle, |1\rangle\}$. We obtain an average gate fidelity of $\bar{F}_1 = 99.68 \pm 0.15\%$ and an average Trotter error of $\bar{\mathcal{E}}_1 = 0.12 \pm 0.04\%$ at 1000 Trotter steps. The polynomial fit shows a scaling behaviour of $\bar{\mathcal{E}}_1 \approx A_1 \times \Delta t^{\nu_1}$, with $\nu_1 = 1.89$ and $A_1 = 566$.

In addition to producing the energy spectrum with high accuracy, the VQE and VQD algorithms prepare the initial states needed for simulating desired quantum gates. As a proof of concept, we simulate the bit-flip gate operation, which transforms the computational state $|0\rangle$ to $|1\rangle$ and vice versa. Since the transmon is a multi-level quantum system with small anharmonicity between its successive energy levels (see Fig. 2(b)), resonantly driving the two lowest energy levels can, in principle, populate multiple higher energy levels, resulting in undesired leakage. To overcome this problem, the derivative removal by adiabatic gate (DRAG) scheme [41, 75, 76] is applied (see Appendix E). Trotterized evolution of the DRAG gate involving 1000 Trotter steps is numerically simulated and its results can be seen in Fig. 3(a). An upper bound of 304 gates is determined for a single Trotter step. We observe from Fig. 3(a) that the population in the ground state is reliably transferred to the excited state within a gate time of $t_g = 85.32$ ns, minimizing leakage to other undesired states.

In order to evaluate the performance of the aforementioned Trotterized bit-flip gate operation, we prepare 300 Haar random initial states, sampled from the Bloch sphere spanned by $\{|0\rangle, |1\rangle\}$, and evolve them both numerically exactly and under the Trotterized digital quantum circuit for various Trotter step sizes. The average gate fidelity (see Appendix F) is found to be $\bar{F}_1 = 99.68 \pm 0.15\%$. It is limited by remaining population in the ground state and can be increased by further optimization of the gate parameters. The average Trotter error at the gate time t_{g1} is $\bar{\mathcal{E}}_1 = 0.12 \pm 0.04\%$ at 1000 Trotter steps. In Fig. 3(b), we show that the Trotter error decreases polynomially with Trotter step size $\Delta t = \frac{t}{K}$. The extracted error scaling $\bar{\mathcal{E}}_1 \propto \Delta t^{\nu_1}$ with $\nu_1 = 1.89$ is superlinear and thus more favorable than the linear theoretical upper bound in Eq. (6). Therefore, although the cumulative gate count places such simulations beyond the near-term regime, the Trotter error of single-qubit DRAG gates scales well with step size and does not appear to suffer from the time dependence of the gate Hamiltonian.

We remark that our optimized variational quantum circuits from the VQE and VQD algorithms can be used to prepare either the $|0\rangle$ or $|1\rangle$ initial state of the transmon, whereas superpositions of the form $a|0\rangle + b|1\rangle$, with $a, b \in \mathbb{C}$ and $|a|^2 + |b|^2 = 1$ are required to estimate the average gate fidelity and simulation error. However, existing techniques such as the linear combination of unitary gates method [77] can be applied to prepare an arbitrary superposition state from the VQE and VQD circuits. We leave the quantum circuit implementation of this kind to future work.

B. Two-qubit cell design

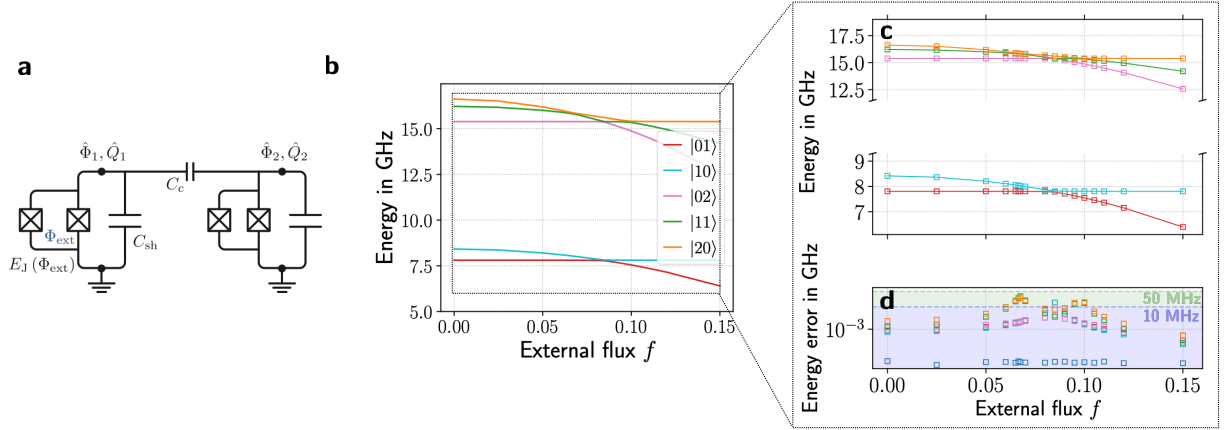


FIG. 4. (a) Circuit diagram of two frequency tunable transmons coupled via a capacitor. (b) The lowest five excited state energies, with respect to the ground state energy, are plotted as a function of the external flux $f_1 = \Phi_{ext,1}/\Phi_0$ threading the left transmon, while the second external flux $f_2 = 0$ is held constant. The solid lines are the exact diagonalization result, where each \hat{N}_i and $\hat{\varphi}_i$ is truncated to $d = 16$ levels and $i = 1, 2$. The states $|01\rangle, |10\rangle, |02\rangle, |11\rangle, |20\rangle$ denote the approximate eigenstates of the combined system when both transmons are far detuned. The avoided level crossings at $f_1 \approx 0.6$ and $f_1 \approx 0.8$ correspond to the operating windows for the CPHASE and i SWAP gates, respectively (see the main text for details). (c) The VQE- and VQD-optimized excitation energies (colored markers) are plotted over the exact diagonalization result. (d) The absolute energy differences between the VQE or VQD calculations and the exact diagonalization are shown versus f_1 . The blue and green shaded regions indicate regions of error below 10 MHz and 50 MHz, respectively.

The design of a device that is capable of quantum computation requires two-qubit simulations en route to scaling to a larger processor size. Although we have already found the energy spectrum of an individual transmon, the spectrum has to be updated when two or more transmons are coupled together via capacitors such as in the circuit in Fig. 4(a). Here we set Josephson energies of $E_J/h = 22$ GHz (left transmon) and $E_J/h = 19$ GHz (right transmon), capacitances of $C_{sh} + C_J = 91$ fF for both transmons, and a coupling capacitance of $C_c = 0.5$ fF. The Hilbert space dimension has now doubled and eight data qubits are required for quantum simulations instead of the previous number of four. The system Hamiltonian is given in Eq. (3). Since the two transmons interact via the coupling capacitor, one expects to see avoided level crossings in the energy spectrum, which are essential in the development of many two-transmon quantum gates. We note that we use capacitive coupling as an example and our methods are also applicable to other transmon-transmon interaction schemes such as inductive coupling [78].

To estimate eigenenergies of the two-transmon system, we again apply the VQE and VQD algorithms. Here, the ansatz used for simulating two transmon qubits comprises two blocks of the four-qubit circuit template used in the single-transmon case, followed by an eight-qubit circuit template (see Fig. D.3(c)). Parameters for the two four-qubit blocks are first optimized assuming a system of individual *uncoupled* transmons. These parameter settings are then used to initialize the corresponding parameters to compute energies of the coupled transmons. The VQD estimate of the first five excited state flux spectra with respect to the VQE-optimized ground state energy are shown in Fig. 4(b-c) along with the exact diagonalization result. The normalized external flux f_1 (left transmon) is swept from 0 to 0.15 while $f_2 \approx 0$ (right transmon) is fixed. In the regime where the two transmons are far detuned, the states are labelled as $|01\rangle, |10\rangle, |02\rangle, |11\rangle, |20\rangle$ in order to keep track of how the respective states change and interact with one another at the avoided level crossings. Absolute energy differences between the VQD estimates and the exact diagonalization results are presented in Fig. 4(d). They are found to be below 50 MHz (green shaded region) around the avoided level crossings and below the previously established threshold of 10 MHz (blue shaded region) elsewhere. This shows that variational optimization is harder when the state extends over a larger number of data qubits, and more circuit layers or longer optimization times could be used to reach the 10 MHz error threshold for all flux points.

After performing the VQE and VQD optimizations, the initial states that are required for two-qubit gate simulations have been found. There are two commonly used two-qubit gates for capacitively coupled transmons: CPHASE and i SWAP. Each of them is implemented by tuning the system to a different avoided level crossing (see Fig. 4(b-c)). The first avoided level crossing between the states $|11\rangle$ and $|20\rangle$ enables the CPHASE gate, while the second avoided level crossing between $|01\rangle$ and $|10\rangle$ constitutes the interaction point for the i SWAP gate [8]. For a proof-of-principle numerical experiment, we carry out digital quantum simulation of the more common CPHASE gate operation, which

features less leakage to undesired states. There are two means to realize the gate, one via an adiabatic sweep of the external flux f_1 [12] and another via an instantaneous (or diabatic) change of flux [13]. In this study, we take the latter approach and prepare the system in the $|11\rangle$ state, suddenly tune f_1 close to the avoided level crossing, let $|11\rangle$ and $|20\rangle$ interact for some time, and suddenly change f_1 back to the initial flux point. The interaction imparts a phase on $|11\rangle$ that is different from the other computational states. Post-rotations on the states remove spurious dynamical phases, resulting in a CPHASE operation on the two transmons. A numerical simulation of the digital Suzuki-Trotter algorithm that simulates the diabatic CPHASE gate with 50,000 Trotter steps is shown in Fig. 5(a) for the initial state $|11\rangle$. Oscillations between the states $|11\rangle$ and $|20\rangle$ are observed, while unwanted transitions to other states labelled as “leakage” are suppressed throughout the gate evolution. The gate is completed at the time $t_{g2} = 104.64$ ns when the excitation has returned to the $|11\rangle$ state.

The performance of the exact CPHASE gate is quantified by the average gate fidelity over 900 Haar random initial state samples, which is given by $\bar{F}_2 = 99.5 \pm 0.1\%$ and is comparable to state of the art experimental demonstrations [19]. The average Trotter error over 100 Haar random states amounts to $\bar{\mathcal{E}}_2 = 0.7 \pm 0.4\%$ for 50,000 Trotter steps. We again show that the Trotter error decreases polynomially with the Trotter step size Δt . The simulation data in Fig. 5(b) show an error scaling $\bar{\mathcal{E}}_2 \propto \Delta t^{\nu_2}$ with $\nu_2 = 3.75$ for sufficiently small step sizes. We make two surprising observations: First, the polynomial scaling onset of the Trotter error $\bar{\mathcal{E}}_2$ appears for step sizes below 10^{-4} ns, which is six orders of magnitude below the gate time. For the single-qubit gate simulation in Sec. III A, the step size only needed to be less than four orders below the gate time. A likely cause for the discrepancy lies in the diabatic turn-on of the CPHASE gate interaction, whereas the single qubit pulse is smooth and slow after the rotating frame approximation. Second, the Trotter error scales with almost fourth order in the step size. This rate is much larger than both the linear upper bound given by Eq. (6) and the almost quadratic scaling of the single-qubit gate simulation. Therefore, the Trotter error can be reduced quickly by decreasing the step size once the polynomial onset has been reached.

We note that the presented simulation method is not limited to the specific two-qubit gate implementation discussed here. It can also be applied to more advanced protocols leading to fast and high fidelity gates [79]. In addition, we remark that we implement the Gray encoding scheme subsystem-wise, such that the combined two-transmon system is given by the tensor product of the two single-transmon Gray blocks of four data qubits each.

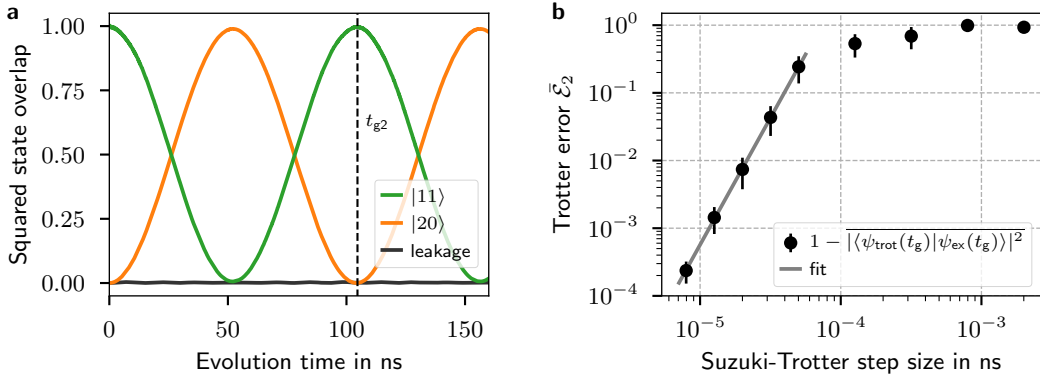


FIG. 5. Digital quantum simulation of a two-transmon CPHASE gate operation. (a) Population of the states $|11\rangle$ and $|20\rangle$ and leakage to other states are plotted versus Trotterized evolution time. One dynamical instance with 50,000 Trotter steps is shown here. The system is initially prepared in the uncoupled $|11\rangle$ state and propagated under the interaction Hamiltonian, which is diabatically switched on. Phase corrections are applied subsequently to obtain the full CPHASE gate. (b) Trotter error $\bar{\mathcal{E}}$ versus Trotter step size Δt . We obtain an average gate fidelity of $\bar{F}_2 = 99.5 \pm 0.1\%$ over 900 Haar random initial states spanned by $\{|00\rangle, |01\rangle, |10\rangle, |11\rangle\}$. For each step size, we perform the CPHASE Suzuki-Trotter evolution over a gate time of $t_{g2} = 104.64$ ns for 100 Haar random initial states spanned by the same computational basis. At 50,000 Trotter steps, the average Trotter error is $\bar{\mathcal{E}}_2 = 0.7 \pm 0.4\%$. The polynomial fit shows a scaling behaviour of $\bar{\mathcal{E}}_2 \approx A_2 \times \Delta t^{\nu_2}$, with $\nu_2 = 3.75$ and $A_2 = 3.2 \times 10^{15}$.

C. Scaling to a multi-qubit sub-module

Based on our study of digital quantum simulation of single- and two-transmon cells, we anticipate that the presented VQE and VQD algorithms to simulate next-generation superconducting quantum devices are a viable application for NISQ (noisy intermediate-scale quantum) processors. In the case of a transmon chain submodule such as the one in Fig. 1(b-c), variational algorithms would shed light on unwanted cross-talk arising from spurious capacitances between any or all transmons in the submodule. Such interactions can be gleaned from the static energy spectra that variational algorithms provide. The relevant metrics for experimental suitability of the variational algorithm are the number of data qubits, circuit depth, and gate count required to simulate an M -transmon processor submodule. Both for near-term quantum computers and for intermediate-scale, partially error-corrected architectures, gate errors and thus simulation errors increase with the number of gates and effects from limited coherence increase with circuit depth. In addition, algorithmic runtime is closely linked to circuit depth for any processor, including error-corrected ones.

In order to simulate M transmons, the circuit ansatz used for the two-transmon simulation in Sec. III B can be naturally extended. Each transmon is again encoded in four data qubits using the Gray code, such that the total data qubit count scales linearly with M rather than exponentially if one were to use a classical computer. The qubit count can be reduced by exploring different encodings or by using less data qubits to represent transmons that are expected to be less relevant for the spectral region of interest. We place two layers of 4-qubit ansatz blocks at the beginning of the variational circuit, connecting each set of four data qubits that encode a single transmon. The next two block layers then connect eight data qubits and we continue to add pairs of ansatz blocks that double the included number of qubits. The final block pair is a $4M$ -qubit ansatz that connects all data qubits. All blocks are extensions of the 4-qubit ansatz from Fig. D.3(b), with single layers of X - and Z -rotation gates at the beginning and end and Mølmer-Sørensen XX gates between each pair of qubits in between. More information on scaling the variational circuit to M transmons and determining the resource counts is provided in Appendix D.

We determine that the gate count and depth of the variational circuit scales favorably with the number of transmons M . The analysis is based on the capabilities of ion trap quantum computers to provide practical context, thereby assuming all-to-all connectivity between the data qubits. At the same time, we emphasize that the methods throughout this work are generally applicable to any digital quantum processor after transformation to the respective native gate set and accounting for connectivity constraints. We find that the total number of 2-qubit gates, which are usually the dominant source of gate errors, is equal to $32M^2 - 4M \log_2(M) - 20M$. The circuit depth depends on the number of gates that can be performed in parallel on the digital quantum processor. In the most optimistic case, XX gates can be performed between arbitrarily many different pairs of data qubits simultaneously. Experimental work by Grzesiak *et al.* [80] suggests that such highly parallelized control capabilities are an emerging capability on ion trap processors. In this scenario, the total depth of the variational circuit scales linearly as $16M + 6 \log_2(M) - 2$. If the 2-qubit gates are not parallelizable at all, the circuit depth scaling increases by one order to that of the gate count. We emphasize that the gate count and circuit depth have sufficiently small prefactors that are compatible with the NISQ regime. Future ion trap devices can be expected to perform some parallelized 2-qubit operations, albeit not to the degree that arbitrarily many 2-qubit gates can be performed at once. The circuit depth would then lie in between the linear and quadratic scaling, and further work is required to assess the additional impact of limited connectivity between distant qubit pairs.

Unlike stationary simulations of the spectrum, the dynamical gate simulations are beyond the reach of near-term devices. The reason is the large number of 304 and 152 entangling gates (upper bound) per single Trotter step to simulate the single-qubit bit-flip gate and the two-qubit CPHASE gate, respectively. The number of gates in the single-qubit simulation is larger than the two-qubit gate simulation because of the DRAG scheme (see Appendix E), in which the Hamiltonian is a function of projection operators instead of sparse matrices. The gate upper bounds are estimated by cancelling adjacent gates in the Suzuki-Trotter evolution, exploiting commutation relations, and simplifying commonly occurring patterns as described in [49]. Afterwards, the remaining CNOT gates are counted. As described in Sec. III, 1000 and 50,000 Trotter steps were applied to digitally quantum simulate the single-transmon bit-flip gate and the two-transmon CPHASE gate, attaining favourable Trotter errors $\mathcal{E}_1 = 0.12 \pm 0.04\%$ and $\mathcal{E}_2 = 0.7 \pm 0.4\%$, respectively. Therefore, a total of 3.04×10^5 CNOT operations is required for the bit-flip gate simulation and 7.6×10^6 CNOT operations for the CPHASE gate simulation. The gate count can in principle be reduced by tolerating a higher Trotter error or by applying existing gate count reduction techniques [81, 82]. Nevertheless, the large gate count places our Suzuki-Trotter simulations of transmon gates in the regime of intermediate-term or even long-term error-corrected quantum computers. When simulating the gate operation of a multi-transmon processor, the Trotter step gate depth must be increased to capture the interactions between the transmons. In our example of a capacitatively coupled sub-module in Fig. 1(c), such interactions are governed by the capacitive interactions between the transmons. As a processor's gate performance typically decreases when parallelizing 2-qubit gates [19, 80], it will also be of relevance to quantum computer-aided design to capture parallel time dynamics of the transmons. The

digital quantum circuits for the respective Trotter steps can be determined with the encoding methods presented in this work, and the resource counts for such simulations are left for future work.

IV. CONCLUSION

The best quantum processors today are already too large to be simulated on any existing classical machine, and they continue to grow at an exponential pace. If one hopes to capture the behavior of design primitives and sub-modules that grow with processor size, future quantum processors will have to be simulated on quantum computers. In this work, we have developed and simulated a detailed set of hybrid classical-quantum algorithms that can be used for quantum computer-aided design. With the use of the variational quantum eigensolver and variational quantum deflation algorithm for near-term quantum processors, we numerically simulated quantum circuits on four and eight data qubits that encode a single transmon and two capacitively coupled transmons, respectively. Errors incurred from running these algorithms are small with respect to the dominant system energy scale. In addition, we were able to prepare transmon eigenstates and pinpoint avoided energy level crossings which are then used to simulate dynamical one- and two-transmon hardware gates with state-of-the-art fidelities. The Suzuki-Trotter gate counts suggest viability of performing these dynamical simulations on intermediate-term quantum hardware, and Trotter errors scale favorably with the Trotter step size. Our work indicates that quantum computer-aided design enables exploration of circuit parameters within the quantum processor sub-module without fabricating and re-designing physical hardware, thereby saving time and cost. In order to have further design control, one may combine our proposed scheme with classical computation methods for superconducting circuit design and simulation [9, 10, 28], thereby benefiting from both classical and quantum computing resources in a single design pipeline. In addition, our methodology of encoding multi-level quantum hardware in data qubits and investigating static and dynamic properties with near- and intermediate-term quantum algorithms provides a general framework that is readily applicable to trapped ion, neutral atom, photonic, and other systems.

ACKNOWLEDGEMENTS

We acknowledge J. Braumüller, M. Degroote, I.D. Kivlichan, M. Krenn, M. Kjaergaard, and G.O. Samach for valuable discussions. T.H.K., T.M., and A.A.-G. acknowledge funding from Intel Research and from Dr. Anders G. Frøseth. T.M. and A.A.-G. also acknowledge the Vannevar Bush Faculty Fellowship under contract ONR N00014-16-1-2008. S.S. is supported by the Department of Energy Computational Science Graduate Fellowship under grant number DE-FG02-97ER25308. A.A.-G. also acknowledges support from the Canada 150 Research Chairs Program, the Canada Industrial Research Chair Program, and from Google, Inc. in the form of a Google Focused Award. The authors declare that there are no competing interests.

Appendix A: Flux qubit design

In the main text, we have presented digital quantum simulations of superconducting transmons. Here we emphasize that our proposed methods are not only limited to transmons but are readily applied to other superconducting qubits as well as other quantum hardware. For this purpose and as a proof of concept, we study another common on-chip circuit design: the radio frequency superconducting quantum interference device (rf-SQUID), which contains a superconducting loop with inductance L , interrupted by a Josephson junction (JJ). In this configuration, a superposition of two magnetic flux states arises: a supercurrent flowing clockwise in the loop and the same amount of current flowing anticlockwise [83]. These currents have been observed experimentally [84, 85]. By inserting multiple JJs in the SQUID loop, a more compact and significantly flux-noise reduced qubit design is obtained [83]. In this context, a commonly adopted design is the three-junction flux qubit, as shown in Fig. A.1(a), consisting of a superconducting loop with small inductance L interrupted by three JJs. The design allows classical bistability even for $L \rightarrow 0$. That enables a weak coupling to magnetic flux noise, resulting in long coherence times [71, 86–88]. The ratio α between the small and large Josephson junctions is typically in the regime $0.5 < \alpha < 1$. The capacitively shunted (C-shunted) flux qubit implemented in Ref. [71] features an additional, large capacitance across the small α -junction as shown in Fig. A.1(b). In addition, the junction asymmetry is chosen to be larger: $\alpha < 0.5$. These modifications, in addition to improved fabrication techniques, have been shown experimentally to increase coherence and decrease process variations of the

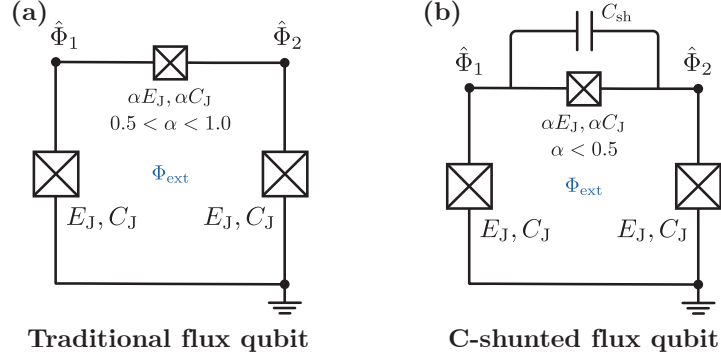


FIG. A.1. Two flux qubit designs considered. (a) A typical three Josephson junction flux qubit, with the smaller α junction in the middle. (b) C-shunted flux qubit with additional large capacitance across the α junction. Each Josephson junction is characterized by Josephson energy E_J , which is the potential energy accumulated in the junction when a supercurrent flows through it, and capacitance C_J .

C-shunted flux qubit over the traditional one [71]. So far, we have summarized variants of flux qubits, with differing circuit components. That means classical equations of motion for each flux qubit design are different, giving rise to distinct Hamiltonians. However, the methods to simulate the different qubit designs are essentially the same. For instance, the C-shunted flux qubit has the following Hamiltonian [71]:

$$\hat{H}_{\text{fq}} = 4 \frac{1 + \alpha + \rho}{1 + 2\alpha + 2\rho} E_{C_J} \left(\hat{N}_1^2 + \hat{N}_2^2 \right) + 8 \frac{\alpha + \rho}{1 + 2\alpha + 2\rho} E_{C_J} \hat{N}_1 \hat{N}_2 - E_J (\cos \hat{\varphi}_1 + \cos \hat{\varphi}_2 + \alpha \cos (2\pi f - \hat{\varphi}_1 + \hat{\varphi}_2)). \quad (\text{A1})$$

Here, α is the junction size ratio, $\rho = C_{\text{sh}}/C_J$, and f is an applied magnetic flux in units of flux quanta Φ_0 . Operators in the above Hamiltonian satisfy the commutation relation $[\hat{\varphi}_j, \hat{N}_k] = i\delta_{jk}$, with δ_{jk} being the Kronecker delta. The operator $\hat{\varphi}_j$ denotes the flux operator associated with the node j in the circuit, as shown in Fig. A.1. We note that the Hamiltonians for the three JJ flux qubit and C-shunted flux qubit differ only in the prefactors of the terms in Eq. (A1). By changing some system parameters, in this case the capacitance across the small α JJ, we can convert from one design to the other. Their respective energy spectra are shown in Fig. A.2.

Appendix B: Physical qubit Hamiltonians in the charge number bases

With the commutation relation $[\hat{\varphi}_j, \hat{N}_k] = i\delta_{jk}$ from Appendix A, one can show the relations

$$[\widehat{e^{i\varphi_j}}, \hat{N}_j] = -\widehat{e^{i\varphi_j}}, \quad \widehat{e^{\pm i\varphi_j}} |n_j\rangle = |n_j \pm 1\rangle, \quad (\text{B1})$$

where $|n_j\rangle$ are the eigenstates of \hat{N}_j . We notice that the operators $\widehat{e^{\pm i\varphi_j}}$ are similar to the usual bosonic creation and annihilation operators, without the square root pre-factor. They are, in fact, the Susskind-Glogower phase operators [89]. When we write down the Hamiltonian \hat{H}_{fq} of the flux qubit in the charge number basis, we use Eq. (B1) and assign the operators as:

$$\hat{N} = \sum_{n=0}^{d-1} \left(n - \frac{d}{2} \right) |n\rangle \langle n|, \quad (\text{B2})$$

$$\cos \hat{\varphi} = \frac{1}{2} \sum_{n=0}^{d-2} (|n\rangle \langle n+1| + |n+1\rangle \langle n|), \quad (\text{B3})$$

$$\sin \hat{\varphi} = \frac{i}{2} \sum_{n=0}^{d-2} (|n\rangle \langle n+1| - |n+1\rangle \langle n|). \quad (\text{B4})$$

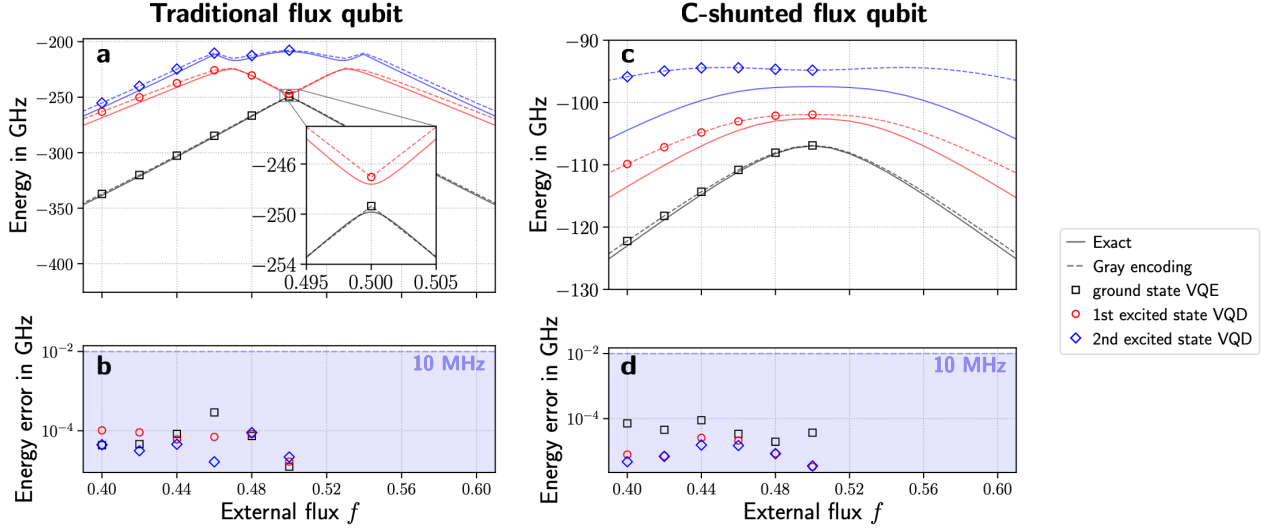


FIG. A.2. (a) Three lowest VQE- and VQD-optimized energies (colored markers) and the exact diagonalization results (solid and dashed lines) of the traditional flux qubit are plotted against external flux f . (b) The absolute energy differences between VQE/VQD calculations and exact values are plotted against f . The blue shaded regions indicate regions of errors below 10 MHz. (c) Four lowest VQE- and VQD-optimized excited energies (colored markers) and the exact diagonalization results (solid and dashed lines) of the C-shunted flux qubit are plotted against external flux f . (d) The absolute energy differences between VQE/VQD calculations and exact values are plotted against f . We remark that in (a) and (c), solid lines correspond to the results obtained from exact diagonalization of the respective Hamiltonian written in the charge basis with $d = 11$ truncation for each active node in the circuit while the dashed lines represent exact diagonalization results with $d = 9$ truncation for each of the nodes. The VQE and VQD simulations are performed with six data qubits, three for each active node in the circuit, corresponding to a truncation of $d = 2^3 = 8$ for each active node.

In general, the number of Cooper pairs can take on infinitely many integer values. However, for practical purposes, we are only interested in low lying energy states. In that case, we can truncate the Hilbert space as described above by introducing a finite maximum number of excitations $d = 2^k$, $k \in \mathbb{N}$. The number of data qubits used in the quantum simulation of the flux qubit is k .

Appendix C: Encoding of quantum operators into Pauli strings

In order to represent the superconducting circuit or any other type of d -level bosonic quantum hardware in terms of qubit states, we convert the eigenstates of the number operator \hat{N} into the computational basis states of k data qubits by representing the integer charge number in a preferred encoding [49, 90, 91]. This implies a truncation of the physical space to the subspace spanned by 2^k Cooper pair numbers. There are combinatorially many ways to map such a state space to a set of qubits. For all the numerical quantum simulation experiments presented throughout this work, we have employed the Gray code [49] due to its resource efficient representation of tridiagonal quantum matrix operators. After integer labeling, each level is encoded into a set of bits, which is then mapped to Pauli operators:

$$\begin{aligned} |0\rangle\langle 1| &= (X + iY)/2, \\ |1\rangle\langle 0| &= (X - iY)/2, \\ |0\rangle\langle 0| &= (\mathbb{I} + Z)/2, \\ |1\rangle\langle 1| &= (\mathbb{I} - Z)/2. \end{aligned}$$

Here, X, Y, Z are the usual Pauli matrices and \mathbb{I} is the identity. Encodings for the operators seen in Eqs. (2, 3, A1) truncated at $d = 8$ and $d = 16$ are given in Tables C.1 and C.2, respectively. In terms of required two-data-qubit operations, the operator \hat{N} is most efficient in the standard binary representation, but operators $\cos \hat{\varphi}$ and $\sin \hat{\varphi}$ are most efficient in the Gray representation. Overall, the Gray code is superior, assuming one performs the Trotterization in only one encoding. However, if one converts between the standard binary and Gray encodings, using the former for \hat{N} and the latter for the other two operators may be a more efficient approach during Trotterization [49].

| $d = 8$ | Std. Binary | Gray | Unary |
|----------------------|--|--|--|
| \hat{N} | $-0.5 I$ $-2.0 Z_2$ $-1.0 Z_1$ $-0.5 Z_0$ | $-0.5 I$ $-2.0 Z_2$ $-1.0 Z_1 Z_2$ $-0.5 Z_0 Z_1 Z_2$ | $-2.0 I + 2.0 Z_0$ $+1.5 Z_1 + 1.0 Z_2$ $+0.5 Z_3 - 0.5 Z_5$ $-1.0 Z_6 - 1.5 Z_7$ |
| $\cos \hat{\varphi}$ | $+0.5 X_0$ $+0.25 X_0 X_1$ $+0.25 Y_0 Y_1$ $+0.125 X_0 X_1 X_2$ $+0.125 X_0 Y_1 Y_2$ $+0.125 Y_0 X_1 Y_2$ $-0.125 Y_0 Y_1 X_2$ | $+0.5 X_0$ $+0.25 X_1$ $-0.25 Z_0 X_1$ $+0.125 X_2$ $-0.125 Z_1 X_2$ $+0.125 Z_0 X_2$ $-0.125 Z_0 Z_1 X_2$ | $+0.25 X_0 X_1 + 0.25 Y_0 Y_1$ $+0.25 X_1 X_2 + 0.25 Y_1 Y_2$ $+0.25 X_2 X_3 + 0.25 Y_2 Y_3$ $+0.25 X_3 X_4 + 0.25 Y_3 Y_4$ $+0.25 X_4 X_5 + 0.25 Y_4 Y_5$ $+0.25 X_5 X_6 + 0.25 Y_5 Y_6$ $+0.25 X_6 X_7 + 0.25 Y_6 Y_7$ |
| $\sin \hat{\varphi}$ | $-0.5 Y_0$ $-0.25 X_0 Y_1$ $+0.25 Y_0 X_1$ $-0.125 X_0 X_1 Y_2$ $+0.125 X_0 Y_1 X_2$ $+0.125 Y_0 X_1 X_2$ $+0.125 Y_0 Y_1 Y_2$ | $-0.5 Y_0 Z_1 Z_2$ $-0.25 Y_1 Z_2$ $+0.25 Z_0 Y_1 Z_2$ $-0.125 Y_2$ $+0.125 Z_1 Y_2$ $-0.125 Z_0 Y_2$ $+0.125 Z_0 Z_1 Y_2$ | $-0.25 X_0 Y_1 + 0.25 Y_0 X_1$ $-0.25 X_1 Y_2 + 0.25 Y_1 X_2$ $-0.25 X_2 Y_3 + 0.25 Y_2 X_3$ $-0.25 X_3 Y_4 + 0.25 Y_3 X_4$ $-0.25 X_4 Y_5 + 0.25 Y_4 X_5$ $-0.25 X_5 Y_6 + 0.25 Y_5 X_6$ $-0.25 X_6 Y_7 + 0.25 Y_6 X_7$ |

TABLE C.1. Qubit encodings (standard binary, Gray code, and Unary) of elementary operators used in this study, with a truncation of $d = 8$.

To give an explicit example, for the case of the single flux qubit Hamiltonian in Eq. (A1), we truncate the Hilbert space to eight charge states per node, which corresponds to three data qubits per node. The effect of truncation can be seen in Fig. A.2. The solid lines correspond to exact diagonalization of the respective Hamiltonian written in the charge basis with $d = 11$ states for each active node, while the dashed lines use $d = 9$ states per node. Although we use a sub-optimal truncation for the VQE/VQD algorithms, we still obtain good agreement with the more accurate $d = 11$ exact diagonalization result in the flux qubit operation regime around the sweet spot at $f = 0.5$. The deviation is much more pronounced away from the sweet spot.

Appendix D: Variational ansatz for VQE and VQD simulations

We use the variational quantum eigensolver approach to find the static energy spectra of superconducting circuits on near-term quantum hardware. Here we provide the parameterized quantum circuit templates used for all VQE and VQD simulations reported throughout this work. The template is shown in Fig. D.3(a). The “unit” layer of this circuit, inspired by the circuit template used in Ref. [72] and the circuit structure realizing “quantum circuit Born machines” (QCBM) [92], comprises an initial layer of single-qubit rotation gates followed by sequences of Mølmer-Sørensen (XX) gates and another layer of single-qubit rotation gates. Each XX entangling gate is defined as $XX_{ij}(\theta) = \exp(-i\theta X_i X_j/2)$ for qubits i and j . For the two flux qubit systems discussed in Appendix A, five of such unit layers for the six-qubit version of the ansatz were used to approximate the ground and excited states. For the transmon qubit systems, shown in Fig. 2 and Fig. 4, two unit layers for a four-qubit version of the QCBM-inspired ansatz followed by a single unit layer of the eight-qubit version were employed, as shown in Fig. D.3(b) and (c).

Scaling of the variational ansatz with transmon number

We investigate how the variational circuit depth and gate count scale with the number of transmons that are simulated. These are important metrics for the experimental viability of the circuit, as gate errors increase with the number of (mainly 2-qubit) gates and effects from limited coherence increase with circuit depth. This is the case both for near-term and for intermediate-scale, partially error-corrected architectures. In addition, algorithmic runtime is closely linked to circuit depth for any processor, including error-corrected ones. The gate counts and circuit depths

| $d = 16$ | Std. Binary | Gray | Unary |
|-------------------|--|--|--|
| \hat{N} | $-0.5 I$ $-4.0 Z_3$ $-2.0 Z_2$ $-1.0 Z_1$ $-0.5 Z_0$ | $-0.5 I$ $-4.0 Z_3$ $-2.0 Z_2 Z_3$ $-1.0 Z_1 Z_2 Z_3$ $-0.5 Z_0 Z_1 Z_2 Z_3$ | $-4.0 I + 4.0 Z_0$ $+3.5 Z_1 + 3.0 Z_2$ $+2.5 Z_3 + 2.0 Z_4$ $+1.5 Z_5 + 1.0 Z_6$ $+0.5 Z_7 - 0.5 Z_9$ $-1.0 Z_{10} - 1.5 Z_{11}$ $-2.0 Z_{12} - 2.5 Z_{13}$ $-3.0 Z_{14} - 3.5 Z_{15}$ |
| $\cos \hat{\phi}$ | $+0.5 X_0$ $+0.25 X_0 X_1$ $+0.25 Y_0 Y_1$ $+0.125 X_0 X_1 X_2$ $+0.125 X_0 Y_1 Y_2$ $+0.125 Y_0 X_1 Y_2$ $-0.125 Y_0 Y_1 X_2$ $+0.0625 X_0 X_1 X_2 X_3$ $+0.0625 X_0 X_1 Y_2 Y_3$ $+0.0625 X_0 Y_1 X_2 Y_3$ $-0.0625 X_0 Y_1 Y_2 X_3$ $+0.0625 Y_0 X_1 X_2 Y_3$ $-0.0625 Y_0 X_1 Y_2 X_3$ $-0.0625 Y_0 Y_1 X_2 X_3$ $-0.0625 Y_0 Y_1 Y_2 Y_3$ | $+0.5 X_0$ $+0.25 X_1$ $-0.25 Z_0 X_1$ $+0.125 X_2$ $-0.125 Z_1 X_2$ $+0.125 Z_0 X_2$ $-0.125 Z_0 Z_1 X_2$ $+0.0625 X_3$ $-0.0625 Z_2 X_3$ $+0.0625 Z_1 X_3$ $-0.0625 Z_1 Z_2 X_3$ $+0.0625 Z_0 X_3$ $-0.0625 Z_0 Z_2 X_3$ $+0.0625 Z_0 Z_1 X_3$ $-0.0625 Z_0 Z_1 Z_2 X_3$ | $+0.25 X_0 X_1 + 0.25 Y_0 Y_1$ $+0.25 X_1 X_2 + 0.25 Y_1 Y_2$ $+0.25 X_2 X_3 + 0.25 Y_2 Y_3$ $+0.25 X_3 X_4 + 0.25 Y_3 Y_4$ $+0.25 X_4 X_5 + 0.25 Y_4 Y_5$ $+0.25 X_5 X_6 + 0.25 Y_5 Y_6$ $+0.25 X_6 X_7 + 0.25 Y_6 Y_7$ $+0.25 X_7 X_8 + 0.25 Y_7 Y_8$ $+0.25 X_8 X_9 + 0.25 Y_8 Y_9$ $+0.25 X_9 X_{10} + 0.25 Y_9 Y_{10}$ $+0.25 X_{10} X_{11} + 0.25 Y_{10} Y_{11}$ $+0.25 X_{11} X_{12} + 0.25 Y_{11} Y_{12}$ $+0.25 X_{12} X_{13} + 0.25 Y_{12} Y_{13}$ $+0.25 X_{13} X_{14} + 0.25 Y_{13} Y_{14}$ $+0.25 X_{14} X_{15} + 0.25 Y_{14} Y_{15}$ |
| $\sin \hat{\phi}$ | $-0.5 Y_0$ $-0.25 X_0 Y_1$ $+0.25 Y_0 X_1$ $-0.125 X_0 X_1 Y_2$ $+0.125 X_0 Y_1 X_2$ $+0.125 Y_0 X_1 X_2$ $+0.125 Y_0 Y_1 Y_2$ $-0.0625 X_0 X_1 X_2 Y_3$ $+0.0625 X_0 X_1 Y_2 X_3$ $+0.0625 X_0 Y_1 X_2 X_3$ $+0.0625 Y_0 X_1 X_2 X_3$ $+0.0625 Y_0 X_1 Y_2 Y_3$ $+0.0625 Y_0 Y_1 X_2 Y_3$ $-0.0625 Y_0 Y_1 Y_2 X_3$ | $-0.5 Y_0 Z_1 Z_2 Z_3$ $-0.25 Y_1 Z_2 Z_3$ $+0.25 Z_0 Y_1 Z_2 Z_3$ $-0.125 Y_2 Z_3$ $+0.125 Z_1 Y_2 Z_3$ $-0.125 Z_0 Y_2 Z_3$ $+0.125 Z_0 Z_1 Y_2 Z_3$ $-0.0625 Y_3$ $+0.0625 Z_2 Y_3$ $-0.0625 Z_1 Y_3$ $+0.0625 Z_1 Z_2 Y_3$ $-0.0625 Z_0 Y_3$ $+0.0625 Z_0 Z_2 Y_3$ $-0.0625 Z_0 Z_1 Y_3$ $+0.0625 Z_0 Z_1 Z_2 Y_3$ | $-0.25 X_0 Y_1 + 0.25 Y_0 X_1$ $-0.25 X_1 Y_2 + 0.25 Y_1 X_2$ $-0.25 X_2 Y_3 + 0.25 Y_2 X_3$ $-0.25 X_3 Y_4 + 0.25 Y_3 X_4$ $-0.25 X_4 Y_5 + 0.25 Y_4 X_5$ $-0.25 X_5 Y_6 + 0.25 Y_5 X_6$ $-0.25 X_6 Y_7 + 0.25 Y_6 X_7$ $-0.25 X_7 Y_8 + 0.25 Y_7 X_8$ $-0.25 X_8 Y_9 + 0.25 Y_8 X_9$ $-0.25 X_9 Y_{10} + 0.25 Y_9 X_{10}$ $-0.25 X_{10} Y_{11} + 0.25 Y_{10} X_{11}$ $-0.25 X_{11} Y_{12} + 0.25 Y_{11} X_{12}$ $-0.25 X_{12} Y_{13} + 0.25 Y_{12} X_{13}$ $-0.25 X_{13} Y_{14} + 0.25 Y_{13} X_{14}$ $-0.25 X_{14} Y_{15} + 0.25 Y_{14} X_{15}$ |

TABLE C.2. Qubit encodings (standard binary, Gray code, and Unary) of elementary operators used in this study, with a truncation of $d = 16$. In our numerical experiments, we utilize the Gray code.

are determined with trapped ion quantum processors in mind such that they have a practically relevant meaning. At the same time, the methods throughout this work are generally applicable to any digital quantum processor after transformation to the respective native gate set and accounting for connectivity constraints.

We consider the variational simulation of an M -transmon processor, where M is chosen as a power of two for simplicity. The two-transmon variational circuit ansatz from Fig. D.3(c) can then be naturally extended: We place two layers of 4-qubit ansatz blocks at the beginning of the circuit, connecting each set of four data qubits that encode a single transmon. The next two block layers then connect eight data qubits and we continue to add ansatz block pairs that double the included number of qubits. The final block pair is an k_{\max} -qubit ansatz, where $k_{\max} = 4M$ is the number of data qubits required to encode all transmons. All blocks are the natural extension of the 4-qubit ansatz from Fig. D.3(b), with single layers of X - and Z - rotation gates at the beginning and end and XX gates between each pair of qubits in between. We note that in contrast to the variational circuit ansatzes from the one- and two-transmon

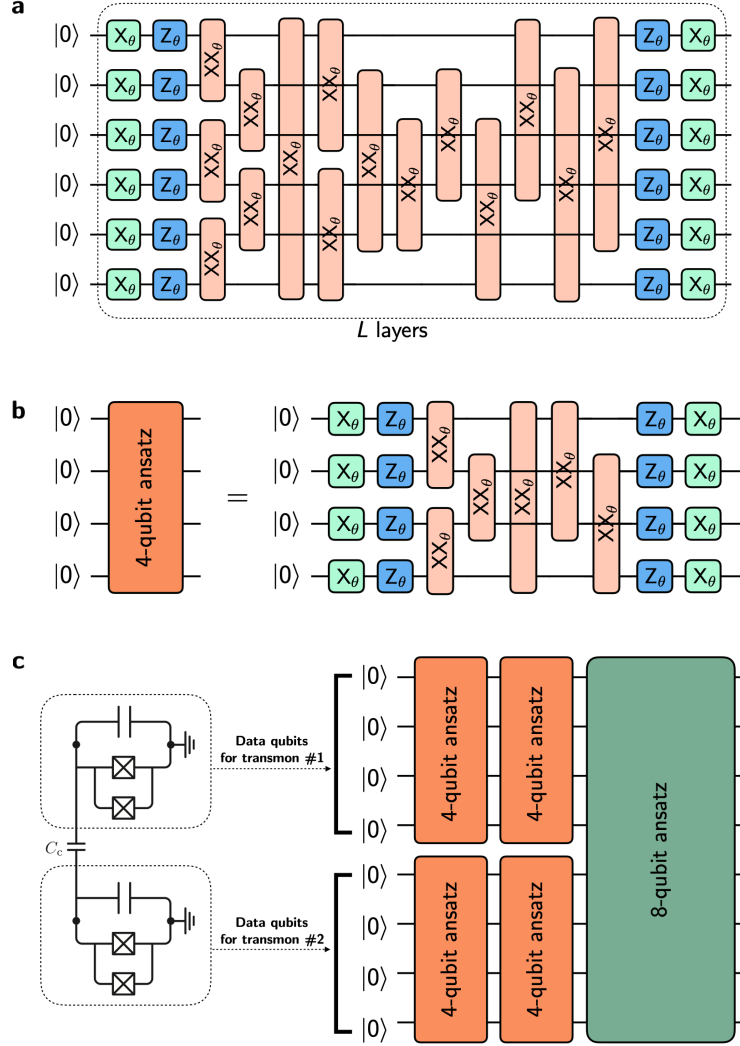


FIG. D.3. Parameterized quantum circuits used to compute spectra of superconducting circuit architectures. (a) Six-qubit version of the parameterized quantum circuit structure used for VQE and VQD simulations of qubit designs investigated in the study of flux qubit designs. The dotted box around the circuit denotes a unit layer, which can be repeated L times to potentially generate a more expressible circuit. (b) Four-qubit version of the circuit structure used to simulate a single transmon. Two unit layers of this four-qubit ansatz were employed in simulations. (c) To simulate two capacitively coupled transmons (shown on the left), we leverage the pre-optimized four-qubit ansatz layers from single transmon simulations and append an eight-qubit ansatz block to capture the interactions between the two transmons. By using results from single transmon simulations, this avoids using a greater number of costly eight-qubit ansatz layers.

simulations, the final block is also repeated in order to simplify the analysis. Additional block layers can easily be accounted for by scaling the gate or depth count with an appropriate scalar prefactor.

We determine the total number of XX gates required for the variational ansatz. As two-qubit gates are usually more error-prone, single-qubit gates are not included in the analysis. The number of single-qubit gates also scales at most with the same order in transmon number as the number of two-qubit gates. Starting from the gate count of each individual block, we notice that a block of k data qubits, where k is a power-of-two multiple of four, has $\frac{k(k-1)}{2}$ unique pairs of qubits. We sum the number of XX gates per block over all blocks in the variational circuit and find the following total number of XX gates:

$$n_{XX}(M) = 32M^2 - 4M \log_2(M) - 20M. \quad (D1)$$

Therefore, the number of entangling gates scales quadratically with the number of transmons, which is viable for a

near-term algorithm.

The overall circuit depth of the variational circuit depends on the number of XX gates that can be performed in parallel on the digital quantum processor. Here we discuss two scenarios, in which (A) XX gates can be performed between arbitrarily many different pairs of qubits simultaneously, or (B) XX gates within a block are sequential but they can be parallel if they are in different blocks. We start with the first scenario, which is inspired by the experimental work by Grzesiak *et al.* [80] that suggests that simultaneous XX gates between arbitrary pairs is an emerging capability on ion trap processors. For a single block, there are always two layers of single-qubit gates (X - and Z -rotations) at the beginning and end, as seen in Fig. D.3(a-b). We then need to find the minimum number of steps to apply XX gates between each pair of qubits. This step number is equivalent to the count of 1-factors of a complete graph with k vertices. By Baranyai's theorem [93], this count is given by $k - 1$. Thus, the depth of a k -qubit ansatz block is given by $k + 3$, after accounting for the depths of single-qubit rotation layers. The total depth $d_A(M)$ of the variational circuit for M transmons is then found by summing over successive blocks:

$$d_A(M) = 16M + 6\log_2(M) - 2.$$

We note that the linear scaling of the circuit depth is advantageous for near-term implementations.

Finally, we discuss the more conservative scenario (B) in which XX gates within a block have to be performed sequentially. This constraint is motivated by the common experimental issue that simultaneous gates lead to undesired cross-talk between the different pairs of ions, particularly in the case of overlapping pairs. It is still assumed that two-qubit gates in different blocks can be applied at the same time, as the respective pairs would be farther away from each other or could be stored in separate sub-modules of a modular ion trap processor [94]. While the four single-qubit layers per k -qubit ansatz block remain the same, the $\frac{k(k-1)}{2}$ two-qubit gates are performed in sequence. By summing the depths of successive blocks as before, we find the following total depth of the M -transmon variational circuit:

$$d_B(M) = \frac{64}{3}M^2 - 8M + 8\log_2(M) + \frac{20}{3}.$$

The scaling of the circuit depth therefore increases by an order in M if two-qubit gates within a block have to be performed successively. In the even more conservative case that no two-qubit gates on the processor can be executed in parallel, the depth scales as the total number of XX gates $n_{XX}(M)$ from Eq. (D1), i.e. still quadratically in M but with a larger prefactor. We expect that future ion trap devices will be able to perform some parallelized two-qubit operations, albeit not at the degree assumed in scenario (A). The circuit depth would then lie in between the two scenarios, and further work is required to assess the additional impact of limited connectivity between distant qubit pairs.

Appendix E: Many-level transmon and the DRAG scheme

Unitary gate operation for a single transmon system is non-trivial and it ought to be discussed briefly here. In this section, we derive the driven transmon Hamiltonian that is simulated in Sec. III A for the bit-flip operation. For concreteness, we focus on the single-transmon bit-flip gate or NOT gate, which can be attained by driving the resonator line capacitively coupled to a transmon. The way to realize the NOT gate in general is to drive the two lowest energy levels with an external field that is resonant with their energy difference. However, the transmon level structure has weak anharmonicity (see Fig. 2(b)). Simply driving the two lowest energy levels would populate higher energy levels, thus reducing the gate fidelity. In order to overcome this issue, the derivative removal by adiabatic gate (DRAG) scheme [41, 75, 76] is applied and the corresponding result can be seen in the main text Fig. 3. The idea of the DRAG scheme is to use two slowly varying quadrature controls to instantaneously cancel leakages to undesired levels such as transitions to second and third excited states.

The combined system and drive Hamiltonian can be modelled ($\hbar = 1$) as

$$\begin{aligned} \hat{H}_{\text{gate}} &= \hat{H}_{1\text{-transmon}} + \hat{H}_{\text{resonator}} + \hat{H}_{\text{interaction}} + \hat{H}_{\text{drive}} \\ &= \sum_{j=1}^{d-1} (j\omega_1 + \Delta_j) |j\rangle\langle j| + \omega \hat{b}^\dagger \hat{b} + \sum_{j=1}^{d-1} \left[g_{j,j-1} |j\rangle\langle j-1| \hat{b} + g_{j-1,j} |j-1\rangle\langle j| \hat{b}^\dagger \right] + \epsilon(t)(\hat{b} + \hat{b}^\dagger), \end{aligned} \quad (\text{E1})$$

where ω_1 is the energy gap between the ground and first excited state of the transmon and Δ_j are the energy level anharmonicities, with $\Delta_1 = 0$, $\Delta_2 = \omega_2 - 2\omega_1$, and $\Delta_n = \omega_n - n\omega_1$, where ω_j is the eigenenergy of the eigenstate $|j\rangle$, i.e. $\hat{H}_1|j\rangle = \omega_j|j\rangle$. The frequency of the single mode resonator is given by ω . The operator $\hat{b}^\dagger(\hat{b})$ is the bosonic creation (annihilation) operator of the resonator, while $g_{j,k}$ is the light-matter coupling strength between the resonator

mode and a specific transmon level transition $|j\rangle\langle k|$. The time-dependent external drive amplitude of the resonator quadrature is given by $\epsilon(t)$. In the above notation, we take the ground state energy to be zero for the projector $|0\rangle\langle 0|$. We also define the projectors $\hat{P}_j = |j\rangle\langle j|$. Assuming weak driving and tracing out the resonator degree of freedom, the drive Hamiltonian can be well approximated as [75]

$$\hat{H}_{\text{drive}} = \epsilon(t) \sum_{j=1}^{d-1} \lambda_{j-1} \hat{\mathcal{P}}_{j-1,j}^x. \quad (\text{E2})$$

We have $\lambda_0 = 1$, and the λ_j can be treated as input parameters. In the numerical simulations presented in the main text, for simplicity, the transmon is assumed to be in the nonlinear oscillator regime with $\lambda_j \approx \sqrt{j}$ and $\lambda_0 = 1$. Subscripts j refer to the j th eigenenergy state and we defined the projector $\hat{\mathcal{P}}_{j,k}^x = |j\rangle\langle k| + |k\rangle\langle j|$. For a circuit QED system, one needs to properly take into consideration couplings between the resonator mode and the particular eigenstate of the transmon to arrive at the correct λ_j 's and $\epsilon(t)$ [75]. For simplicity, let us take

$$\epsilon(t) = \Omega_x(t) \cos(\omega_d t + \phi_0) + \Omega_y(t) \sin(\omega_d t + \phi_0) \quad (\text{E3})$$

as the external driving field with frequency ω_d . The relative phase between the envelope and the carrier at the start of the operation is given by ϕ_0 . In a rotating frame given by

$$\hat{K}(t) = \sum_{j=1}^{d-1} \exp(-ij\omega_d t) \hat{P}_j, \quad (\text{E4})$$

we arrive at

$$\begin{aligned} \hat{H}'_{\text{gate}} &= \hat{K}^\dagger(t) \hat{H}_{\text{gate}} \hat{K}(t) + i\dot{\hat{K}}^\dagger(t) \hat{K}(t) \\ &= \sum_{j=1}^{d-1} (j\delta(t) + \Delta_j) \hat{P}_j + \sum_{j=1}^{d-1} \lambda_{j-1} \left[\frac{\Omega_x(t)}{2} \hat{\mathcal{P}}_{j-1,j}^x + \frac{\Omega_y(t)}{2} \hat{\mathcal{P}}_{j-1,j}^y \right] \end{aligned} \quad (\text{E5})$$

after the rotating wave approximation. Here, $\hat{\mathcal{P}}_{j,k}^y = -i|j\rangle\langle k| + i|k\rangle\langle j|$ and $\delta(t) = \omega_1(t) - \omega_d$. Ideally, the above Hamiltonian generates a unitary evolution

$$\hat{\mathcal{U}} = \mathcal{T} \exp \left[-i \int_0^{t_g} \hat{H}'_{\text{gate}}(t) dt \right] = e^{i\phi_0} \hat{\mathcal{U}}_{\text{qubit}} \oplus \hat{\mathcal{U}}_{\text{rest}}. \quad (\text{E6})$$

For a leakage-free qubit [41, 75, 76], we require $\delta(t) = \Omega_y(t) = 0$. The Gaussian modulated envelope [75]

$$\Omega_x(t) = A \left(\frac{\exp \left[\frac{-(t-t_g/2)^2}{2\sigma^2} \right] - \exp \left(-\frac{t_g^2}{8\sigma^2} \right)}{\sqrt{2\pi\sigma^2} \operatorname{erf} \left(\frac{t_g}{\sqrt{8}\sigma} \right) - t_g \exp \left(-\frac{t_g^2}{8\sigma^2} \right)} \right) \quad (\text{E7})$$

is chosen such that it starts and ends at zero. The parameter t_g refers to the gate time, while σ is the standard deviation of the Gaussian distribution. In the limit $t_g \rightarrow \infty$, it recovers the standard Gaussian distribution function. The only requirement here is that $\int_0^{t_g} \Omega_x(t) dt = \pi$, since we want a bit-flip gate. Hence, $A = \pi$. Lastly, we note that Eq. (E5) is the Hamiltonian we use to digitally simulate the bit-flip gate in our numerical experiment seen in Fig. 3.

Appendix F: Average gate fidelity

As seen in the main text and in Sec. E, due to the weak anharmonicity and multi-level nature of the transmon, there is undesired leakage during the single- and two-transmon gate evolution. In general, leakage is modeled by describing the system of interest as a subsystem of a larger Hilbert space governed by unitary evolution. Hence, one can label d_1 energy levels where the computational subspace is \mathcal{H}_1 , and all the other energy levels (d_2 -dimensional) are labeled as \mathcal{H}_2 . For example, a single transmon has $\mathcal{H}_1 \in \{|0\rangle, |1\rangle\}$, while two transmons have $\mathcal{H}_1 \in \{|00\rangle, |01\rangle, |10\rangle, |11\rangle\}$. The d_2 -dimensional subspace of all additional levels that the system may arrive at due to some leakage dynamics can be called the leakage subspace. The total state space is $(d_1 + d_2)$ -dimensional and denoted as $\mathcal{H} = \mathcal{H}_1 + \mathcal{H}_2$.

With leakage, we would like to quantify how our unitary gate evolution performs. This is done using the average gate fidelity [95, 96], defined as

$$\bar{F} = \int_{\psi_1 \in \mathcal{H}_1} d\psi_1 \text{Tr} \left(\hat{U} |\psi_1\rangle\langle\psi_1| \hat{U}^\dagger \hat{\mathcal{G}} [|\psi_1\rangle\langle\psi_1|] \right) \approx \frac{1}{\mathcal{M}} \sum_{i=1}^{\mathcal{M}} \text{Tr} \left(\hat{U} |\psi_1^{(i)}\rangle\langle\psi_1^{(i)}| \hat{U}^\dagger \hat{\mathcal{G}} [|\psi_1^{(i)}\rangle\langle\psi_1^{(i)}|] \right), \quad (\text{F1})$$

where $\hat{U} = \hat{U}_{\text{des}}$ is a unitary map and $\hat{\mathcal{G}}$ is a general linear, trace-preserving quantum channel acting on an initial pure state $|\psi_1\rangle\langle\psi_1|$. In the context of this work, $\hat{\mathcal{G}} = \hat{U}_{\text{ex}}$ (left hand side of Eq. (6)). The integral is over the uniform (Haar) measure $d\psi_1$ over the computational subspace \mathcal{H}_1 , normalized to $\int d\psi_1 = 1$. A fidelity of $\bar{F} = 1$ would mean that \hat{U} implements $\hat{\mathcal{G}}$ perfectly.

-
- [1] G. G. E. Gielen and R. A. Rutenbar, “Computer-aided design of analog and mixed-signal integrated circuits,” *Proc. IEEE* **88**, 1825 (2000).
 - [2] F. L. Cox, W. B. Kuhn, J. P. Murray, and S. D. Tynor, “Code-level modeling in xspice,” *Proc. IEEE International Symposium on Circuits and Systems* **2**, 871 (1992).
 - [3] T. Tuma and A. Buermen, *Circuit simulation with SPICE OPUS: theory and practice* (Springer, 2009).
 - [4] T. Austin, E. Larson, and D. Ernst, “Simplescalar: An infrastructure for computer system modeling,” *Computer* **35**, 59 (2002).
 - [5] E. Larson, S. Chatterjee, and T. M. Austin, “Mase: a novel infrastructure for detailed microarchitectural modeling,” *Proc. IEEE Intl Symp. Performance Analysis of Systems and Software (ISPASS-2001)* **1**, 9 (2001).
 - [6] G. Burkard, R. H. Koch, and D. P. DiVincenzo, “Multilevel quantum description of decoherence in superconducting qubits,” *Phys. Rev. B* **69**, 064503 (2004).
 - [7] U. Vool and M. Devoret, “Introduction to quantum electromagnetic circuits,” *Int. J. Circ. Theor. App.* **45**, 897 (2017).
 - [8] P. Krantz, M. Kjaergaard, F. Yan, T. P. Orlando, S. Gustavsson, and W. D. Oliver, “A quantum engineer’s guide to superconducting qubits,” *Appl. Phys. Rev.* **6**, 021318 (2019).
 - [9] T. Menke, F. Häse, S. Gustavsson, A. J. Kerman, W. D. Oliver, and A. Aspuru-Guzik, “Automated discovery of superconducting circuits and its application to 4-local coupler design,” [arXiv:1912.03322](https://arxiv.org/abs/1912.03322) (2019).
 - [10] G. Li, Y. Ding, and Y. Xie, “Towards efficient superconducting quantum processor architecture design,” [arXiv:1911.12879](https://arxiv.org/abs/1911.12879) (2019).
 - [11] A. A. Houck, J. Schreier, B. Johnson, J. Chow, J. Koch, J. Gambetta, D. Schuster, L. Frunzio, M. Devoret, S. Girvin, *et al.*, “Controlling the spontaneous emission of a superconducting transmon qubit,” *Phys. Rev. Lett.* **101**, 080502 (2008).
 - [12] L. DiCarlo, J. M. Chow, J. M. Gambetta, L. S. Bishop, B. R. Johnson, D. Schuster, J. Majer, A. Blais, L. Frunzio, S. Girvin, *et al.*, “Demonstration of two-qubit algorithms with a superconducting quantum processor,” *Nature* **460**, 240 (2009).
 - [13] L. DiCarlo, M. D. Reed, L. Sun, B. R. Johnson, J. M. Chow, J. M. Gambetta, L. Frunzio, S. M. Girvin, M. H. Devoret, and R. J. Schoelkopf, “Preparation and measurement of three-qubit entanglement in a superconducting circuit,” *Nature* **467**, 574 (2010).
 - [14] R. Barends, J. Kelly, A. Megrant, A. Veitia, D. Sank, E. Jeffrey, T. C. White, J. Mutus, A. G. Fowler, B. Campbell, *et al.*, “Superconducting quantum circuits at the surface code threshold for fault tolerance,” *Nature* **508**, 500 (2014).
 - [15] J. Kelly, R. Barends, A. G. Fowler, A. Megrant, E. Jeffrey, T. C. White, D. Sank, J. Y. Mutus, B. Campbell, Y. Chen, *et al.*, “State preservation by repetitive error detection in a superconducting quantum circuit,” *Nature* **519**, 66 (2015).
 - [16] A. Kandala, A. Mezzacapo, K. Temme, M. Takita, M. Brink, J. M. Chow, and J. M. Gambetta, “Hardware-efficient variational quantum eigensolver for small molecules and quantum magnets,” *Nature* **549**, 242 (2017).
 - [17] J. Otterbach, R. Manenti, N. Alidoust, A. Bestwick, M. Block, B. Bloom, S. Caldwell, N. Didier, E. S. Fried, S. Hong, *et al.*, “Unsupervised machine learning on a hybrid quantum computer,” [arXiv:1712.05771](https://arxiv.org/abs/1712.05771) (2017).
 - [18] M. Gong, M.-C. Chen, Y. Zheng, S. Wang, C. Zha, H. Deng, Z. Yan, H. Rong, Y. Wu, S. Li, *et al.*, “Genuine 12-qubit entanglement on a superconducting quantum processor,” *Phys. Rev. Lett.* **122**, 110501 (2019).
 - [19] F. Arute, K. Arya, *et al.*, “Quantum supremacy using a programmable superconducting processor,” *Nature* **574**, 505 (2019).
 - [20] H. Meuer, E. Strohmaier, J. Dongarra, H. Simon, and M. Meuer, “Top500 list of most powerful commercially available computer systems,” <https://www.top500.org>, accessed 25 March 2020.
 - [21] K. De Raedt, K. Michielsen, H. De Raedt, B. Trieu, G. Arnold, M. Richter, T. Lippert, H. Watanabe, and N. Ito, “Massively parallel quantum computer simulator,” *Comput. Phys. Commun.* **176**, 121 (2007).
 - [22] M. Smelyanskiy, N. P. Sawaya, and A. Aspuru-Guzik, “qHiPSTER: the quantum high performance software testing environment,” [arXiv:1601.07195](https://arxiv.org/abs/1601.07195) (2016).
 - [23] T. Häner and D. S. Steiger, “0.5 petabyte simulation of a 45-qubit quantum circuit,” *Proceedings of the International Conference for High Performance Computing, Networking, Storage and Analysis* **33**, 1 (2017).
 - [24] T. Monz, D. Nigg, E. A. Martinez, M. F. Brandl, P. Schindler, R. Rines, S. X. Wang, I. L. Chuang, and R. Blatt, “Realization of a scalable Shor algorithm,” *Science* **351**, 1068 (2016).

- [59] Y. Shen, X. Zhang, S. Zhang, J.-N. Zhang, M.-H. Yung, and K. Kim, “Quantum implementation of the unitary coupled cluster for simulating molecular electronic structure,” *Phys. Rev. A* **95**, 020501 (2017).
- [60] C. Hempel, C. Maier, J. Romero, J. McClean, T. Monz, H. Shen, P. Jurcevic, B. P. Lanyon, P. Love, R. Babbush, A. Aspuru-Guzik, R. Blatt, and C. F. Roos, “Quantum Chemistry Calculations on a Trapped-Ion Quantum Simulator,” *Phys. Rev. X* **8**, 031022 (2018).
- [61] Y. Nam, J.-S. Chen, N. C. Pienti, K. Wright, C. Delaney, D. Maslov, K. R. Brown, S. Allen, J. M. Amini, J. Apisdorf, K. M. Beck, A. Blinov, V. Chaplin, M. Chmielewski, C. Collins, S. Debnath, A. M. Ducore, K. M. Hudek, M. Keesan, S. M. Kreikemeier, J. Mizrahi, P. Solomon, M. Williams, J. D. Wong-Campos, C. Monroe, and J. Kim, “Ground-state energy estimation of the water molecule on a trapped ion quantum computer,” [arXiv:1902.10171](#) (2019).
- [62] J. I. Colless, V. V. Ramasesh, D. Dahlen, M. S. Blok, M. E. Kimchi-Schwartz, J. R. McClean, J. Carter, W. A. de Jong, and I. Siddiqi, “Computation of Molecular Spectra on a Quantum Processor with an Error-Resilient Algorithm,” *Phys. Rev. X* **8**, 011021 (2018).
- [63] J. McClean, N. Rubin, K. Sung, I. D. Kivlichan, X. Bonet-Monroig, Y. Cao, C. Dai, E. S. Fried, C. Gidney, B. Gimby, P. Gokhale, T. Haner, T. Hardikar, V. Havlíček, O. Higgott, C. Huang, J. Izaac, Z. Jiang, X. Liu, S. McArdle, M. Neeley, T. O’Brien, B. O’Gorman, I. Ozfidan, M. D. Radin, J. Romero, N. P. D. Sawaya, B. Senjean, K. Setia, S. Sim, D. S. Steiger, M. Steudtner, Q. Sun, W. Sun, D. Wang, F. Zhang, and R. Babbush, “OpenFermion: The electronic structure package for quantum computers,” *Quantum Sci. Technol.* (2020), [10.1088/2058-9565/ab8ebc](#).
- [64] R. S. Smith, M. J. Curtis, and W. J. Zeng, “A Practical Quantum Instruction Set Architecture,” [arXiv:1608.03355](#) (2016).
- [65] J. R. Johansson, P. Nation, and F. Nori, “QuTiP: An open-source python framework for the dynamics of open quantum systems,” *Comp. Phys. Comm.* **183**, 1760 (2012).
- [66] N. Wiebe, D. Berry, P. Hoyer, and B. C. Sanders, “Higher order decompositions of ordered operator exponentials,” *J. Phys. A-Math. Theor.* **43**, 065203 (2010).
- [67] G. G. Guerreschi, J. Hogaboam, F. Baruffa, and N. Sawaya, “Intel Quantum Simulator: A cloud-ready high-performance simulator of quantum circuits,” [arXiv:2001.10554](#) (2020).
- [68] I. D. Kivlichan, C. Gidney, D. W. Berry, N. Wiebe, J. McClean, W. Sun, Z. Jiang, N. Rubin, A. Fowler, A. Aspuru-Guzik, *et al.*, “Improved fault-tolerant quantum simulation of condensed-phase correlated electrons via trotterization,” [arXiv:1902.10673](#) (2019).
- [69] G. H. Low and N. Wiebe, “Hamiltonian simulation in the interaction picture,” [arXiv:1805.00675](#) (2018).
- [70] D. Poulin, A. Qarry, R. Somma, and F. Verstraete, “Quantum simulation of time-dependent Hamiltonians and the convenient illusion of Hilbert space,” *Phys. Rev. Lett.* **106**, 170501 (2011).
- [71] F. Yan, S. Gustavsson, A. Kamal, J. Birenbaum, A. P. Sears, D. Hover, T. J. Gudmundsen, D. Rosenberg, G. Samach, S. Weber, J. L. Yoder, T. P. Orlando, J. Clarke, A. J. Kerman, and W. D. Oliver, “The flux qubit revisited to enhance coherence and reproducibility,” *Nat. comm.* **7**, 12964 (2016).
- [72] P. B. M. Sousa and R. V. Ramos, “Universal quantum circuit for n-qubit quantum gate: A programmable quantum gate,” [arXiv:quant-ph/0602174](#) (2006).
- [73] S. Sim, P. D. Johnson, and A. Aspuru-Guzik, “Expressibility and Entangling Capability of Parameterized Quantum Circuits for Hybrid Quantum-Classical Algorithms,” *Adv. Quantum Technol.* **2**, 1900070 (2019).
- [74] R. H. Byrd, P. Lu, J. Nocedal, and C. Zhu, “A Limited Memory Algorithm for Bound Constrained Optimization,” *SIAM J. Sci. Comput.* **16**, 1190 (1995).
- [75] J. M. Gambetta, F. Motzoi, S. T. Merkel, and F. K. Wilhelm, “Analytic control methods for high-fidelity unitary operations in a weakly nonlinear oscillator,” *Phys. Rev. A* **83**, 012308 (2011).
- [76] A. De, “Fast quantum control for weakly nonlinear qubits: On two-quadrature adiabatic gates,” [arXiv:1509.07905](#) (2015).
- [77] A. M. Childs and N. Wiebe, “Hamiltonian simulation using linear combinations of unitary operations,” *Quantum Inf. Comput.* **12**, 901 (2012).
- [78] Y. Chen, C. Neill, P. Roushan, N. Leung, M. Fang, R. Barends, J. Kelly, B. Campbell, Z. Chen, B. Chiaro, *et al.*, “Qubit architecture with high coherence and fast tunable coupling,” *Phys. Rev. Lett.* **113**, 220502 (2014).
- [79] M. Rol, F. Battistel, F. Malinowski, C. Bultink, B. Tarasinski, R. Vollmer, N. Haider, N. Muthusubramanian, A. Bruno, B. Terhal, and L. DiCarlo, “Fast, high-fidelity conditional-phase gate exploiting leakage interference in weakly anharmonic superconducting qubits,” *Phys. Rev. Lett.* **123**, 120502 (2019).
- [80] N. Grzesiak, R. Blümel, K. Beck, K. Wright, V. Chaplin, J. M. Amini, N. C. Pienti, S. Debnath, J.-S. Chen, and Y. Nam, “Efficient arbitrary simultaneously entangling gates on a trapped-ion quantum computer,” [arXiv:1905.09294](#) (2019).
- [81] A. M. Childs, A. Ostrander, and Y. Su, “Faster quantum simulation by randomization,” *Quantum* **3**, 182 (2019).
- [82] E. Campbell, “Random compiler for fast hamiltonian simulation,” *Phys. Rev. Lett.* **123**, 070503 (2019).
- [83] T. P. Orlando, J. E. Mooij, L. Tian, C. H. Van Der Wal, L. S. Levitov, S. Lloyd, and J. J. Mazo, “Superconducting persistent-current qubit,” *Phys. Rev. B* **60**, 15398 (1999).
- [84] J. R. Friedman, V. Patel, W. Chen, S. K. Tolpygo, and J. E. Lukens, “Quantum superposition of distinct macroscopic states,” *Nature* **406**, 43 (2000).
- [85] D. Vion, A. Aassime, A. Cottet, P. Joyez, H. Pothier, C. Urbina, D. Esteve, and M. H. Devoret, “Manipulating the quantum state of an electrical circuit,” *Science* **296**, 886 (2002).
- [86] I. Chiorescu, Y. Nakamura, C. J. P. M. Harmans, and J. E. Mooij, “Coherent quantum dynamics of a superconducting flux qubit,” *Science* **299**, 1869 (2003).
- [87] E. Il’ichev, N. Oukhanski, A. Izmailkov, T. Wagner, M. Grajcar, H.-G. Meyer, A. Y. Smirnov, A. M. van den Brink, M. H. S. Amin, and A. M. Zagoskin, “Continuous monitoring of rabi oscillations in a josephson flux qubit,” *Phys. Rev. Lett.* **91**, 097906 (2003).

- [88] P. Bertet, I. Chiorescu, G. Burkard, K. Semba, C. J. P. M. Harmans, D. P. DiVincenzo, and J. E. Mooij, “Relaxation and dephasing in a flux-qubit,” [arXiv:cond-mat/0412485](#) (2004).
- [89] L. Susskind and J. Glogower, “Quantum mechanical phase and time operator,” *Physics Physique Fizika* **1**, 49 (1964).
- [90] L. Veis, J. Viřňák, H. Nishizawa, H. Nakai, and J. Pittner, “Quantum chemistry beyond Born–Oppenheimer approximation on a quantum computer: A simulated phase estimation study,” *Int. J. Quantum Chem.* **116**, 1328 (2016).
- [91] S. McArdle, A. Mayorov, X. Shan, S. Benjamin, and X. Yuan, “Digital quantum simulation of molecular vibrations,” *Chem. Sci.* **10**, 5725 (2019).
- [92] M. Benedetti, D. Garcia-Pintos, O. Perdomo, V. Leyton-Ortega, Y. Nam, and A. Perdomo-Ortiz, “A generative modeling approach for benchmarking and training shallow quantum circuits,” *npj Quantum Inf.* **5**, 45 (2019).
- [93] Z. Baranyai, in *Infinite and Finite Sets, vol. I, Colloquium of Keszthely*, edited by A. Hajnal, R. Rado, and V. Sós (1973).
- [94] C. Monroe and J. Kim, “Scaling the ion trap quantum processor,” *Science* **339**, 1164 (2013).
- [95] M. D. Bowdrey, D. K. L. Oi, A. J. Short, K. Banaszek, and J. A. Jones, “Fidelity of single qubit maps,” *Phys. Lett. A* **294**, 258 (2002).
- [96] C. J. Wood and J. M. Gambetta, “Quantification and characterization of leakage errors,” *Phys. Rev. A* **97**, 032306 (2018).